Summer 2019

Formation of Clot Analogs Between Co-Flow Fluid Streams in a Microchannel Device

Sue-Mae Saw
San Jose State University

FORMATION OF CLOT ANALOGS BETWEEN CO-FLOW FLUID STREAMS IN A MICROCHANNEL DEVICE

A Thesis

Presented to

The Faculty of the Department of Mechanical Engineering

San José State University

In Partial Fulfillment

of the Requirements for the Degree

Master of Science

by

Sue-Mae Saw

August 2019

The Designated Thesis Committee Approves the Thesis Titled

FORMATION OF CLOT ANALOGS BETWEEN CO-FLOW FLUID STREAMS IN A MICROCHANNEL DEVICE

by

Sue-Mae Saw

APPROVED FOR THE DEPARTMENT OF MECHANICAL ENGINEERING

SAN JOSÉ STATE UNIVERSITY

August 2019

Sang-Joon John Lee, Ph.D.	Department of Mechanical Engineering
Anand Ramasubramanian, Ph.D.	Department of Chemical & Materials Engineering
Melinda Simon, Ph.D.	Department of Biomedical Engineering

ABSTRACT

FORMATION OF CLOT ANALOGS BETWEEN CO-FLOW FLUID STREAMS IN A MICROCHANNEL DEVICE

by Sue-Mae Saw

Hemodynamics plays an important role in the formation of blood clots, for which changes in hydrodynamic stresses and transport phenomena can initiate or inhibit the clotting process. The fibrin network is highly influential in the structural mechanics of a clot. This work demonstrated an ability to produce clot analogs at the boundary between co-flow fluid streams, and investigated the dependence of clot shape and density distribution on flow conditions. The time evolution of fibrin clots formed in microchannel flow was investigated using fluorescence imaging. Clots were formed in a polydimethylsiloxane (PDMS) microfluidic device which consisted of a Y-shaped microchannel with two inlets and a single outlet. The clotting region had a cross-section that was 300 μm wide and 12 μm deep. The first inlet introduced fresh frozen plasma (FFP), while the second inlet introduced thrombin. Clot analogs were formed at the interface of these two parallel streams at withdrawal flow rates of 100 nL/min, 200 nL/min, and 400 nL/min. These clots were shown to be insensitive to initial co-flow shear rates, exhibiting similar clot shape and density distribution across the different flow rates. Clots that are formed in such an engineered device provide opportunities to mimic *in vivo* scenarios in which clot density and composition gradients depend on flow conditions.

ACKNOWLEDGMENTS

This work was supported in part by the AHA Institutional Research Enhancement Award (AIREA) program of the American Heart Association (Award 18AIREA33960524) and in part by the Davidson Student Scholars Program of the Charles W. Davidson College of Engineering at San José State University. The μPIV measurements were made possible thanks to a Major Research Instrumentation (MRI) grant from the National Science Foundation (Award #1727072). Fabrication training and support were provided by the Microscale Process Engineering Laboratory at San José State University. I would like to thank Prof. Sang-Joon John Lee for his tireless guidance, support and patience, Prof. Anand Ramasubramanian for the education in clotting mechanisms, Prof. Melinda Simon for the introduction to particle imaging and microfluidics fluid mechanics, Max Kim for microfabrication training and support, Erika Young for laboratory support, Chaitanya Puligundla for imaging and clotting guidance, and my husband, François Bleibel, for his continuous support and explanations on the principles of optics.

TABLE OF CONTENTS

LIST OF TABLES

LIST OF FIGURES

LIST OF SYMBOLS AND ABBREVIATIONS

Symbol	Units	Description
a_f	m	hydrated fibrin fiber radius
$\boldsymbol{F}$	$N \cdot m^{-2}$	body forces per unit area
h	m	channel height
K	-	kurtosis
k	m^2	permeability
L	m	channel length
n	-	number of values
p	Pa	pressure
S	-	skewness
u_x	$m \cdot s^{-1}$	flow direction velocity (x-direction)
$\dot{\gamma}$	s^{-1}	shear rate
θ	°	angle
μ	$Pa \cdot s$	dynamic viscosity
v	$m \cdot s^{-1}$	interstitial fluid velocity
ρ	$kg \cdot m^{-3}$	density
τ	min	first-order exponential time constant
ϕ_f	-	fibrin fiber volume fraction

Abbreviation	Full Spelling
CCD	charge-coupled device
FFP	fresh frozen plasma
FWQM	full width quarter maximum
Nd:YAG	neodymium-doped yttrium aluminum garnet
PBS	phosphate buffered saline
PDMS	polydimethylsiloxane
PIV, μPIV	particle image velocimetry, micron-resolution particle image velocimetry
RBC	red blood cell
SEM	scanning electron microscope
sCMOS	scientific complementary metal–oxide–semiconductor
TF	tissue factor
UV	ultraviolet

1. INTRODUCTION

1.1 Background

Clot analogs are important in biomedical research when developing physiologically relevant models of vascular thrombosis and hemostasis. Unfortunately, existing studies typically involve clots formed in a static environment with relatively homogeneous composition, despite the composition of clinically relevant clots being very diverse with variations in fibrin and red blood cell (RBC) composition [1]. Tissue factor (TF), exposed at the sites of vascular injury, initiates the extrinsic coagulation cascade, ultimately activating prothrombin into thrombin. Thrombin in turn converts fibrinogen to fibrin, which is essential for the stabilization of a clot. Several *in vitro* studies have been conducted to understand the effects of shear rate on blood coagulation initiated by TF or thrombin, and these studies are mentioned in the following sections.

Microfluidic technology enables the manipulation of thrombus composition and behavior through flow field and surface definition for clot initiation [2]. Complex flow patterns induced by pulsatile motion, and rapid accelerations and decelerations can similarly be introduced in microfluidic devices to imitate *in vivo* conditions [3]. Microfluidic devices are typically transparent, which enables visual observation and monitoring of clotting behavior and progression.

1.1.1 Clot Formation and Structure

Virchow's triad describes the three factors of thrombosis which are vessel wall injury, changes in flow dynamics, and hypercoagulability due to blood being rich in clotting

factors [3]–[5]. TF is exposed after vascular damage, ultimately resulting in thrombin generation which is critical for the initiation of clotting. Analytical models, computational studies and experimental investigations of the TF pathway have confirmed that coagulation is triggered in a threshold manner, where an increase in TF binding sites significantly changes the production of thrombin [6], [7].

A blood clot comprises of a branched fibrin network, platelet aggregates and red blood cells, with clot structure being influenced by blood flow forces and transport mechanisms [8]. Mechanical behavior of clots depends heavily on the different polymerization circumstances [9]. Depending on the conditions of fibrin formation, there is variation in structural and mechanical properties of a clot [10]. Typical vasculature shear rates are less than 200 s^{-1} in veins, greater than 500 s^{-1} in arteries, and between 1000 s^{-1} and 1800 s^{-1} in arterioles [2], [11], [12]. Engineered strain rate micro-gradients provide a way of investigating platelet aggregation regulation [13]–[15]. Roessler et al. performed *in vitro* coagulation at a larger scale for sonothrombolysis applications [16]. This work was able to vary platelet count by altering flow conditions, eventually producing artificial clots that achieved physiologically relevant histological characteristics.

Characterization of tissue can be conducted *in vivo* using pulse wave velocity, or *ex vivo* methods [17]. Often, *ex vivo* mechanical studies on clots involve some form of tensile testing [9], [18], or compression testing [9], [19]. There is a necessity to study the interaction between clot mechanics and hemodynamics through the measurement of clot mechanical properties while being formed under shear flow [20].

1.1.2 Coagulation and Flow Visualization

Coagulation is usually monitored using fluorescence microscopy with visual detection of fluorescence-labeled thrombin generation, fibrin generation, and platelet aggregation [21], [22]. Flow visualization enables direct observation of flow dynamics to assist with better understanding and manipulation of coagulation in microfluidic devices. Micron-resolution particle image velocimetry (μPIV) is a flow visualization technique capable of measuring velocity fields at high temporal and spatial resolutions. The μPIV system developed by Santiago et al. enables the characterization of performance in micron-scale flow systems [23]. In μPIV, flow is seeded with fluorescent tracing microparticles, and discrete images of particle distributions at two instances of time are obtained. Flow velocity is deduced from the particle displacement in a two-dimensional measurement plane within a given time interval. With the implementation of these visualization techniques, the interaction between coagulation and flow dynamics can be investigated.

1.2 Hypothesis

The hypothesis of this investigation is that clot density distribution and shape is insensitive to initial co-flow shear rate.

The rationale for this hypothesis is that once a clot is formed at the co-flow boundary, the dominant factors affecting clot growth are pressure difference across the clot and clot permeability.

1.3 Significance

Venous thromboembolism is life threatening, affecting up to 600,000 Americans yearly [24]. Thrombus formation *in vivo* depends on many factors, and microfluidic devices enable controlled manipulation of these factors to better understand the interplay between prescribed conditions. Clot analogs are conventionally fabricated in a static *in vitro* environment whereas clot formation *in vivo* occurs in the presence of dynamic blood flow. Clot analogs are critical in studies involved in understanding the material and mechanical properties of blood clots, benefiting the development of medical treatments such as mechanical thrombectomy, stent angioplasty, and embolic filtration [25]. This research seeks to synthesize realistic clot analogs at the boundary between active co-flow fluid streams, with the ability to visualize and quantify the effects of flow dynamics on the formation of clot analogs. These clot analogs will better mimic clots found in the human body, assisting with future research concerned with the mechanical properties of human blood clots.

2. RELATED WORK

2.1 Microfluidic Coagulation

Through the observation of human blood and plasma flowing in silica capillaries surface-patterned with patches of TF, the initiation of coagulation has been found to depend on shear rate, and not volumetric flow rate or flow velocity [21]. Coagulation has been seen to have a threshold response to shear rate and size of TF surface patch, where a critical concentration of activated factors is required for the onset of clotting [7]. Hence, a critical surface concentration of TF is required to trigger coagulation under flow, where TF functions at a narrow range between 2 molecules-TF/μm^2 and 20 molecules-TF/μm^2 to initiate platelet and fibrin deposition on collagen at venous shear rates (100 s^{-1}) and arterial shear rates (500 s^{-1} or 1000 s^{-1}). It is similarly recognized that spatial and temporal growth, structure, and mechanical properties of a thrombus are TF surface area and density dependent [26]. The circulation of TF in the flowing blood stream has also been observed to play a contributing role in the propagation of thrombosis [27].

The influence of transport mechanisms on fibrin formation has been observed through a two-channeled membrane-microfluidic device [28]. This device regulated fibrin fiber deposition through thrombin flux and wall shear rate, where fibrin morphology was described in terms of the Peclet and Damkohler numbers. Simultaneous experiments have been conducted in an eight-channel microfluidic device under two modes of operation: constant flow rate or pressure relief conditions, to study the role of fibrin in clot stability [29]. The investigation of blood clot growth, stability and embolization for venous and

arterial shear rates established that clot strength increased up to 28-fold with the presence of fibrin, and 2-fold more fibrin formed under pressure relief mode in venous flow.

2.2 Characterization of Coagulation and Clots

As mentioned in Section 1.1.2, coagulation can be monitored with the assistance of fluorescence microscopy. Fluorescence intensities of fibrin and platelets have been used to quantify the height of clots [26], [29]. The decrease in fluorescence intensity and loss in surface coverage of fluorescently labeled platelets have been correlated with the decrease in clot stability [30]. Apart from extracting intensity values from captured images, fibrin fiber diameter, branches and branching point densities can be determined to characterize changes in fibrin morphology [31].

Besides visual supervision of thrombosis, immunoassays of effluents for prothrombin fragment 1.2, thrombin-antithrombin complex and post-end point plasmin digest from microfluidic thrombosis function as proxies to quantify the transient mass balance of generated thrombin molecules and fibrin monomers in thrombosis [22]. As another option, coagulation can be monitored with an acoustic sensor where resonant frequency measurements decrease as clotting progresses [32]. It is possible to determine the hydraulic permeability of the fibrin network via measurement of interstitial fluid flow within clots at prescribed pressure gradients [33]. Platelet aggregate sizes ascertained through image analysis of fluorescently labeled platelets, and fibrin fiber radii measured by scanning electron microscopy, facilitate permeability computations. Clot permeability has been found to vary by up to five orders of magnitude.

There are various techniques available to determine the mechanical parameters of microtissue through tensile testing. Using a magnetic bead microrheometer, a particle-tracking microrheology technique studied the viscoelastic properties of human fibrin and plasma clots [34]. Three stress relaxation mechanisms of fibrin were observed, and the presence of factor XIII, the effect of fibrinogen, thrombin and calcium concentration levels and the role of fibrinogen γ' on the viscoelastic behavior of clots were investigated using this technique. Laser tweezers particle-tracking microrheology paired with confocal reflection imaging have similarly been used to characterize fibrin hydrogel [35]. Alternatively, the mechanical properties of fibrin networks have been acquired using atomic force microscopy to stretch individual fibrin fibers, and with the assistance of fluorescence microscopy, tensile strain was measured [36]. Tensile testing of microtissues with magnetically actuated microcantilevers has enabled the uncoupled study of cell and matrix effects on the mechanical properties of fibroblast-populated collagen microtissues [37]. A recent work by Chen et al. integrates an elastometry system within a microfluidic device, enabling real-time measurement of clot contraction and clot stiffness as clotting happens under flow conditions [20].

2.3 Co-Flow and Gradient Generating Microfluidic Devices

The capability to precisely achieve and maintain control of *in vitro* microfluidic generated chemical and concentration gradients benefits experiments that mimic non-homogeneities occurring *in vivo*. Gradients can be achieved in a simple two-inlet microchannel or a micromixer array of serpentine channels with each serpentine channel

serving as a diffusion mixing zone within a compact structure [38]. Jeon et al. accomplished two types of gradients using a branched network of serpentine channels, with the first type being solution composition gradients, and the second being surface topography gradients of etch profiles on a silicon dioxide substrate [39]. This branched network design has been further enhanced to involve controlled manipulation of gradients with a range of complex shapes, including linear, parabolic and periodic shapes [40]. Parallel dividers to the direction of flow restrict interdiffusion between two adjacent streams with distinct concentrations, and can be used for the control of gradient generation [41]. With these dividers, any changes in gradient requirements can be accommodated by repositioning the dividers within the channel.

Spatial control of three-dimensional concentration profiles of co-flowing streams has been demonstrated in collagen-filled microchannels with multiple inlets [42]. Microchannel devices with similarly configured co-flow design involving two distinct fluids have been engineered to study the transport and separation of microparticles across laminar flow streams [43], [44]. Making use of three-dimensional particle-tracking techniques and surface reconstruction algorithms, the interface at the co-flow boundary can be reconstructed to assist with research dealing with micromixers [45].

Ability to introduce, modify, and observe constituents within fluid flow expands investigative capability beyond surface-patterned approaches. For instance, Muthard and Diamond performed assays of platelet function in a trifurcated microfluidic device by controlling the interface between citrated whole blood and calcium-containing buffer,

while also removing the corner effects of rectangular microfluidic devices [46]. Limitations of current microfluidic designs for coagulation research are the rectangular channels which have large surface-to-volume ratio, and the edges of rectangular walls which produce flow that are unlike flow within a cylindrical vascular tube [3]. Co-flow fluid infusion also exists as a flow focusing technique. Onasoga-Jarvis et al. used a flow focusing microchannel device consisting of three inlets to focus plasma flow over TF-coated silica beads [47]. Through this device, it was concluded that fibrin deposition depended on a threshold spot size and TF concentration, which in turn depended on shear rate.

A gradient generating microfluidic device provides a platform to study the response of cells to variation in concentration gradients. A microchannel device with three inlets and 22 outlets has been used for bacterial chemotaxis [48]. The response of cells to changes in solutions and concentrations was characterized by the count of accumulated cells in each of the outlet ports. Using a two-channeled membrane-microfluidic device, Kim et al. investigated the activation of Wnt/b-catenin signaling of HeLa cells, which was made possible by a gradient generation chamber consisting of serpentine channels to provide a bipolar environment [49]. This work successfully demonstrated the ability to manipulate stable gradients, while also investigating diffusion- and convection-based flow modes.

Another form of microfluidic gradient involves shear micro-gradients. Primarily shear deceleration has been observed to be critical in the initiation of clotting through platelet

aggregation, both *in vivo* and *in vitro*. This is true even in the absence of clotting factors adenosine diphosphate, thromboxane A_2, and thrombin [15]. Likewise, the criticality of decelerating flow in coagulation activation has been seen in a microfluidic device which mimicked a stenosed arteriole network [14].

2.4 Micron-resolution Particle Image Velocimetry (μPIV) in Blood

Velocity profiles of blood flow in rectangular polydimethylsiloxane (PDMS) channels can be reliably interrogated via μPIV [50]–[52]. The effects of alginate as a viscosity modifier on the behavior of porcine blood proved to have minimal effects on the maximum velocity and flow rate within the channel, however, changes in viscosity had a notable effect of between 8% to 100% on wall shear rate [51]. Research on the link between the velocity profile and blood viscosity variation caused by RBC dispersion, aggregation, and deformation has been similarly conducted *in vivo* and *ex vivo* with the aid of μPIV [53]. Image processing techniques coupled with μPIV enabled the characterization of RBC aggregation based on shear rates obtained from velocity profile measurements [52]. Decreasing shear rates paired with higher hematocrit levels were seen to increase viscosity, hence establishing the shear-thinning behavior of blood. Nevertheless, the increase in aggregation size did not result in a linear increase in the viscosity of blood. The effects of hemodynamics in a stenosed microchannel on platelet aggregation have been similarly visualized and investigated [54]. The implications of dynamic interactions between blood flow through a deformable channel mimicking vasculature wall conditions have been investigated via μPIV of RBCs and 1 μm

fluorescent particles [55]. In this study, it was apparent that RBC velocities were impacted by wall compliance.

μPIV has been adapted for *in vivo* applications permitting the measurement of velocity distribution even within an arteriole in a rat mesentery [56]. An intravital microscope and a high-speed digital video system were used to measure the velocity fields of RBCs, showing a blunt velocity profile in single and straight arterioles. Likewise, the velocity of unsteady blood flow in the beating heart of a chicken embryo has been measured, and shear stress distributions were successfully established within this complex flow geometry [57].

3. THEORY AND SIMULATION

3.1 Fluid Mechanics

Viscous flow is observed in blood vessels, with Stokes flow being observed near the wall, and Poiseuille flow being observed away from the wall [12]. The velocity profile in the direction of flow, $u_x(y, z)$ for Poiseuille flow through a straight rectangular channel for a single fluid is given by equation (3.1) [58], [59]. In this equation, h is the channel height, Δp is the pressure drop across the channel, μ is the fluid dynamic viscosity and L is the channel length. The *xyz*-coordinate system adopted by this work is illustrated in Figure 3.1.

$$u_x(y,z) = \frac{4h^2\Delta p}{\pi^3 \mu L} \sum_{n=1,3,5\ldots}^{\infty} \frac{1}{n^3} \left[1 - \frac{\cosh(n\pi \frac{y}{h})}{\cosh(n\pi \frac{w}{2h})}\right] \sin(n\pi \frac{z}{h}) \tag{3.1}$$

The initiation of the clotting process is sensitive to shear rate, with typical physiological rates ranging from 20 s^{-1} to 1800 s^{-1} [11]. *In vitro* experiments have also been conducted under supra-physiological flow conditions (8000 s^{-1}) in order to test the stability of platelet aggregates formed between shear rates of 100 s^{-1} to 1000 s^{-1} [30]. Blood is described as a non-Newtonian fluid; however, at shear rates greater than 100 s^{-1} blood behaves like a Newtonian fluid. When there are no RBCs present (i.e., 0% hematocrit), plasma also exhibits Newtonian fluid behavior [60]. Shear rate, $\dot{\gamma}$ across the width of the channel is described by equation (3.2) [61].

$$\dot{\gamma} = \frac{1}{2}\frac{\partial u_x}{\partial y} \tag{3.2}$$

The device presented in this work achieves a localized shear zone at the boundary between two flow streams with distinct density and viscosity, involving fresh frozen plasma (FFP) and thrombin, as shown in Figure 3.1 [52]. FFP contains fibrinogen and plasma proteins, while thrombin converts fibrinogen to fibrin. During the clotting experiments, thrombin was diluted in phosphate buffered saline (PBS) to achieve a concentration of 12.5 U/mL. Hence, the fluid properties of the thrombin stream were assumed to be synonymous with the fluid properties of PBS.

The fluid properties are as follows: FFP density, $\rho_1 = 1025\ \text{kg} \cdot \text{m}^{-3}$ [62], FFP dynamic viscosity, $\mu_1 = 0.0015\ \text{Pa} \cdot \text{s}$ [63], PBS density, $\rho_2 = 1000\ \text{kg} \cdot \text{m}^{-3}$, and PBS dynamic viscosity, $\mu_2 = 0.001\ \text{Pa} \cdot \text{s}$. These differences in fluid properties between the two streams result in two distinct velocities in parallel. A single syringe pump that withdraws the fluid at the outlet enforces a constant average flow rate, even though there exists two characteristic velocities in the two parallel streams.

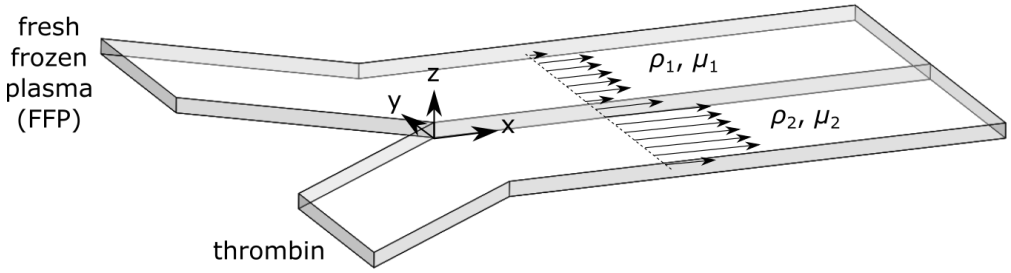

Figure 3.1 Co-flow of FFP and thrombin with differing densities and viscosities.

The presence of distinct velocities in each stream has been reinforced using micron-resolution particle image velocimetry (μPIV, TSI Incorporated, Shoreview, Minnesota, USA). The initial μPIV system by Santiago et al. consisted of an

epifluorescent microscope, an intensified charge-coupled device (CCD) camera and continuous illumination from a mercury lamp [23]. This combination of a continuous light and a CCD camera is only suitable for low-velocity flow measurements, which limits the approaching mean velocity to 35 μm/s [64]. Later on, Meinhart et al. improved illumination by utilizing a double-pulsed Nd:YAG laser [65]. This setup is currently known as the standard μPIV system. A similar setup to this standard μPIV system was used for the μPIV measurements shown in Figure 3.2.

Figure 3.2 presents velocity maps for flow within Y-shaped microchannels at withdrawal flow rates of 100 nL/min and 200 nL/min, respectively. In these maps, FFP flowed along the upper half of the microchannel, and PBS flowed along the lower half of the microchannel. For each measurement, both fluid streams were seeded with 1 μm red fluorescent particles (R0100, Fisher Scientific, Waltham, Massachusetts, USA) at 0.05% concentration. Pure PBS seeded with tracing particles was used at the second inlet to prevent the formation of clots at the co-flow boundary. As expected, these measurements indicate that the thrombin stream would flow at a higher average velocity compared to the FFP stream. From the velocity maps for both flow rates of 100 nL/min and 200 nL/min, it is evident that the distinct average velocities for each fluid stream would result in shearing forces at the boundary.

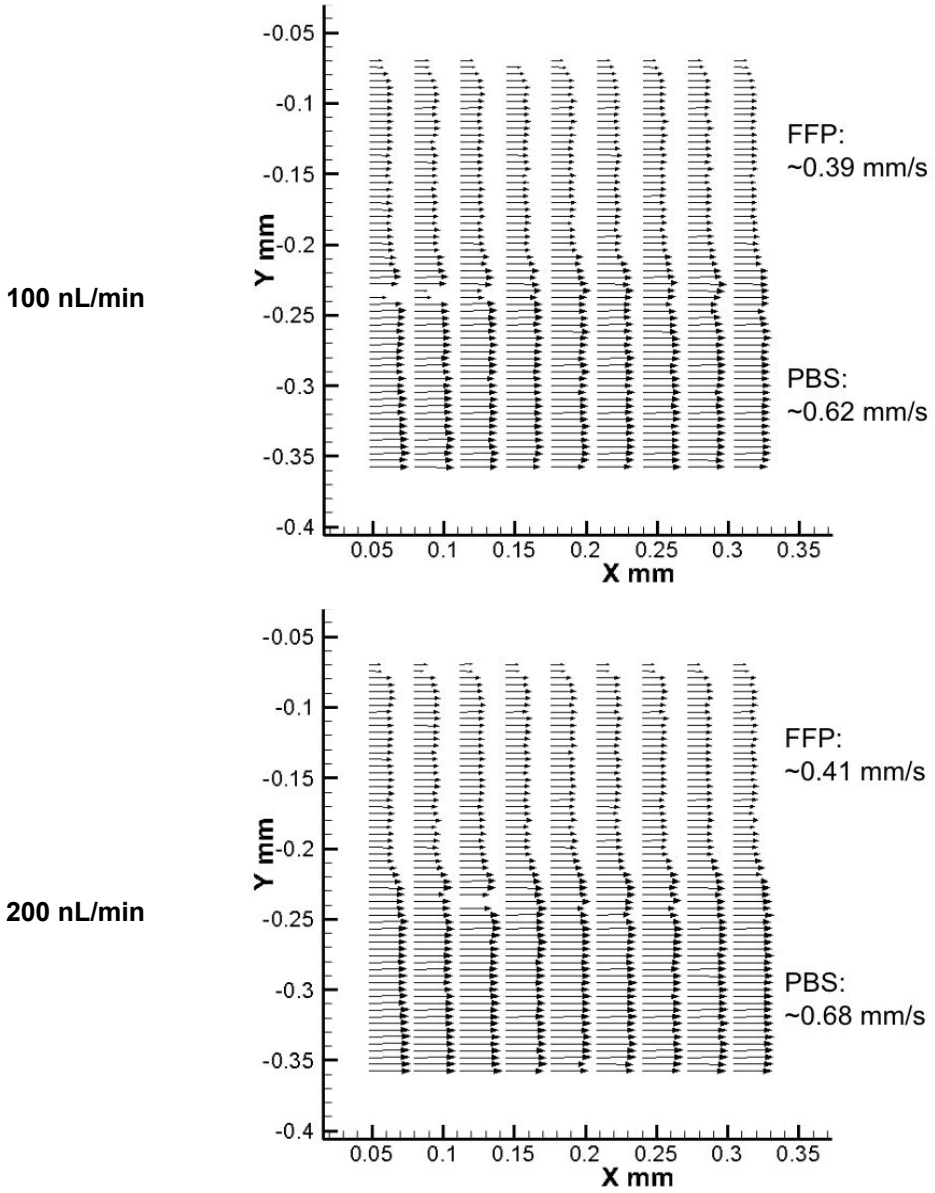

Figure 3.2 μPIV velocity maps.

3.2 Co-Flow Simulation

Simulations were conducted using COMSOL Multiphysics (COMSOL, Inc., Burlington, Massachusetts, USA) to estimate the initial shear rates at the co-flow stream boundaries for volumetric flow rates of 100 nL/min, 200 nL/min and 400 nL/min. All simulations were conducted using a two-dimensional model of the microchannel in the *xy*-plane, at z = 6 μm, to reduce computational loads. A shallow channel approximation was applied to account for the effects of the channel ceiling and floor on fluid flow. A drag term, acting as a body force, was included in the Navier–Stokes equation, as shown in equation (3.3) [66], [67]. $\boldsymbol{F}$ represents any other external body forces acting on the fluid, such as gravity. In these simulations, $\boldsymbol{F}$ amounted to zero. Steady-state and incompressible creeping flow were assumed for all simulations.

$$0 = \nabla \cdot [-\boldsymbol{p} + \mu(\nabla \boldsymbol{u} + (\nabla \boldsymbol{u})^{\mathrm{T}}] - 12\frac{\mu \boldsymbol{u}}{h^2} + \boldsymbol{F} \tag{3.3}$$

The main purpose of these simulations was to predict velocity and shear rate profiles, hence the consideration of the diffusion of species was deemed unnecessary to include within the simulation model. Figure 3.3 shows the fully-developed velocity profile across the microchannel width at z = 6 μm, with FFP flowing along the upper half and thrombin flowing along the lower half of the channel. The presence of distinct velocities is in agreement with the μPIV velocity maps shown in Figure 3.2, along with the theoretical solution and experimental μPIV observations reported by Pitts et al. [68].

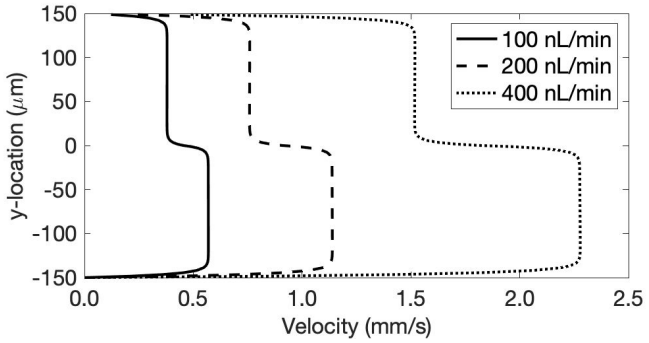

Figure 3.3 Simulated velocity profile across microchannel width at z = 6 μm.

As anticipated, the simulated shear rate is highest at the wall (assuming no-slip condition), as shown in Figure 3.4. There is also a local peak at the interface between fluids. Clot formation was not observed at the channel walls, but was only seen to form at the boundary between the fluid streams where FFP and thrombin met. These simulated results suggest that physiological initial shear rates can be achieved at the fluid interface. Initial shear rates at the stream boundary at z = 6 μm for flow rates of 100 nL/min, 200 nL/min, and 400 nL/min are predicted to be 22.6 s^{-1}, 45.2 s^{-1}, and 90.4 s^{-1}, respectively. It is noted that this model only predicts the initial shear rate at the co-flow boundary. As the clot forms at the boundary, the constant flow rate imposed by the syringe pump subjects the growing clot with increasing shear rates on the surface of the clot [29].

Figure 3.5 shows the pressures across the width of the channel at x = 300 μm and z = 6 μm for withdrawal flow rates of 100 nL/min, 200 nL/min, and 400 nL/min. The pressure differences at various width intervals for all three flow rates, in the y-direction, are shown in Table 3.1.

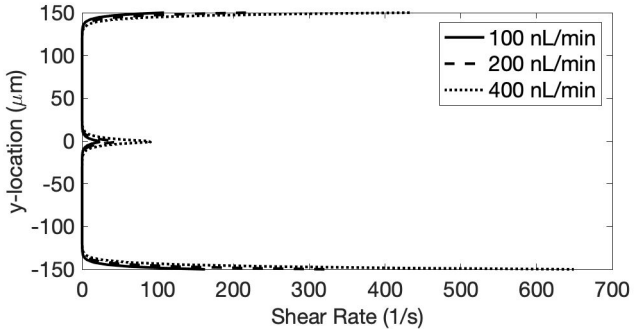

Figure 3.4 Simulated shear rate across microchannel width at z = 6 μm.

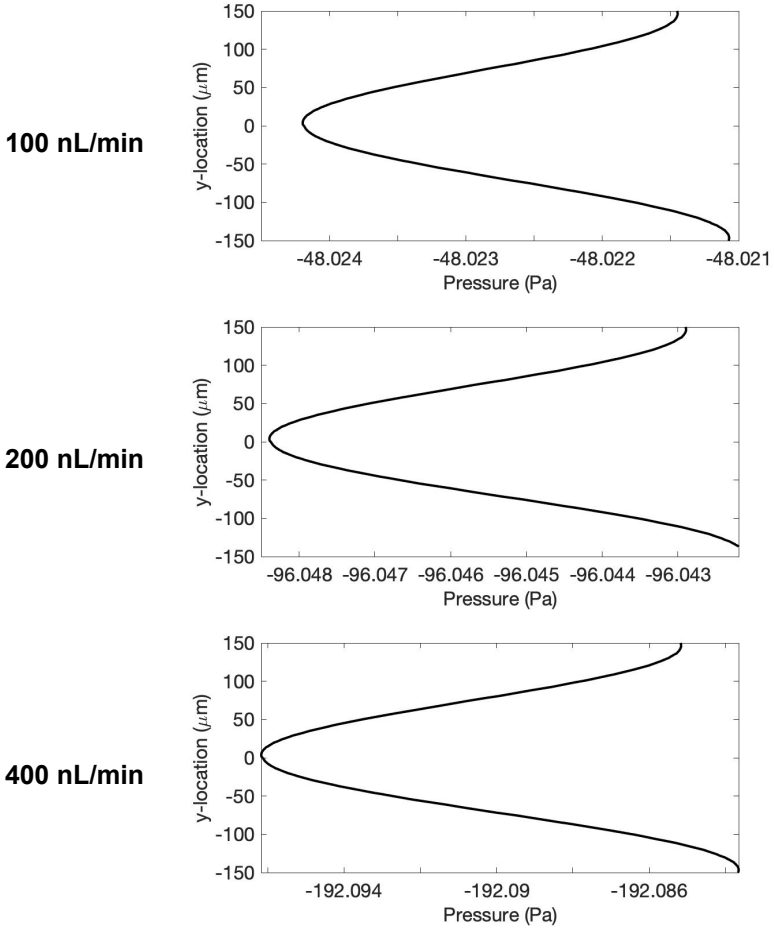

Figure 3.5 Simulated pressure across microchannel width at x = 300 μm, z = 6 μm.

Table 3.1 Pressure Differences Across Microchannel Width at x =300 μm, z = 6 μm

Flow Rate (nL/min)	Pressure Difference (mPa)		
	y = -50 μm to 50 μm	y = -30 μm to 30 μm	y = -10 μm to 10 μm
100	0.10	0.13	0.06
200	0.21	0.26	0.12
400	0.42	0.51	0.23

It is observed that as the interval in the y-direction (e.g., y = -10 μm to 10 μm) converges on the co-flow boundary, the distinction of the pressure difference values decreases between the three flow rates. Hence, as the clot initially forms at the co-flow boundary, it is predicted that the pressure difference across the clot (y-direction) is similar for flow rates between 100 nL/min and 400 nL/min.

3.3 Clot Permeability

A blood clot is essentially a porous medium, and permeability through the clot can be determined from Darcy's law, as shown in equation (3.4) [33]. v is the interstitial fluid velocity, k is permeability, μ is the fluid dynamic viscosity and ∇p is the pressure gradient vector.

$$\nu = -\frac{k}{\mu}\nabla p \tag{3.4}$$

Numerous relationships between permeability in fibrous media have been developed, and have the general form shown in equation (3.5) [33]. a_f is the hydrated fibrin fiber radius, and ϕ_f is the fibrin fiber volume fraction.

$$\frac{k}{{a_f}^2} = f(\phi_f) \tag{3.5}$$

Equations 3.4 and 3.5 show that permeability is impacted by the pressure gradient across the clot and permeability is also a function of fibrin density.

4. METHODOLOGY

4.1 Material Selection, Device Design, and Fabrication

4.1.1 Blood and Material Selection

FFP and thrombin were flowed through a microchannel at room temperature. Aliquots of FFP (Stanford Blood Center, Palo Alto, California, USA) and commercially available thrombin (Catalog Number 69671, MilliporeSigma, Burlington, Massachusetts, USA) were stored at -20 ºC and defrosted at room temperature. Thrombin with concentration of 25 U/mL was diluted with 1X PBS (Gibco 20012050, Fisher Scientific, Waltham, Massachusetts, USA) to achieve a concentration of 12.5 U/mL. To assist with the visualization of fibrin clots, FFP was doped with 5% Alexa Fluor 594-conjugated fibrinogen (F13193, Invitrogen, Waltham, Massachusetts, USA).

4.1.2 Device Design and Fabrication

The formation of clots between co-flow fluid streams requires a Y-channel device, permitting the introduction of FFP and thrombin through separate inlets, to trigger an onset of clotting when the two streams meet. The device must be optically transparent for the visualization of clot formation with an inverted fluorescence microscope. The microchannel design, consisting of a channel 300 μm wide, 12 μm deep, and 10 mm long, is shown in Figure 4.1. FFP was introduced through the top inlet and thrombin was introduced through the bottom inlet.

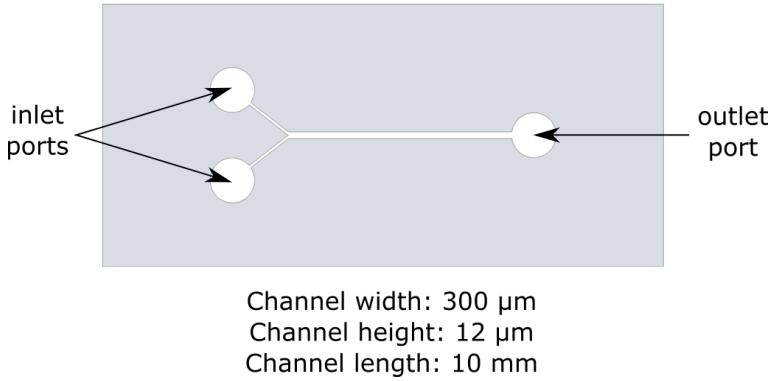

Figure 4.1. Top-view of microfluidic device design.

Soft lithography and PDMS casting techniques, as in [69], were used to fabricate single-use microfluidic devices. SU-8 2007 negative photoresist (MicroChem Corp., Westborough, Massachusetts, USA) was used to fabricate the master mold by selective UV exposure. PDMS was cast on top of the master mold by first mixing and degassing a 10:1 mass ratio of PDMS base resin to curing agent (Sylgard 184, Dow Corning Corp., Midland, Michigan, USA), and then pouring the mixture on top of the master mold to be cured on a hot plate at 100 ºC for 35 min. The outlet port was cored using a 1 mm sampling tool (Harris Uni Core, Electron Microscopy Sciences, Hatfield, Pennsylvania, USA). Inlet ports were cored using a larger 14-gauge stainless steel syringe needle tip to create inlet reservoirs for reagents that were pipetted directly on to the device. The cored PDMS was then plasma-bonded to a glass microscope slide in an inductively-coupled plasma chamber (model PDC-001, Harrick Plasma, Ithaca, New York, USA) at pressures between 300 mTorr to 500 mmTorr, 10 W power, for 60 s. The plasma-bonded chip was annealed on a hot plate at 120 °C for 20 min, then left to cool to ambient temperature.

4.2 Experimentation

4.2.1. Experimental Test Conditions

A total of six experiments were conducted with two replicates at each constant withdrawal flow rate of 100 nL/min, 200 nL/min and 400 nL/min. Before attempting to initiate clotting at the co-flow boundary, PBS was manually withdrawn from both inlets by a manual syringe connected to the outlet port. The microchannel was manually primed to remove any possible air bubbles and debris within the channel. Five μL of pure FFP and 5 μL of pure PBS were then pipetted into each inlet well, and the syringe pump was set to withdraw at 10 μL/min for 1 min. This preparatory step was intended to aid with rapid removal of any hydraulic capacitance within the system, and also to reduce saline dilution from PBS residue left behind by the previous manual withdraw step. The syringe pump was then switched to withdraw at the required flow rate (i.e., 100 nL/min, 200 nL/min, or 400 nL/min) for 10 min to stabilize the flow rate.

After the flow rate had been allowed to stabilize, 10 μL of fluorescently labeled FFP and thrombin, respectively, were pipetted into the inlets alternately at 5 μL increments. Small increments were necessary to reduce unbalanced inlet pressures as a result of differing static heights and droplet size. Immediately after thrombin was introduced into the system, image acquisition of fibrin formation between the co-flow fluid streams commenced. Clots were left to form at a constant withdrawal flow rate for a duration of 20 min.

4.2.2 Apparatus and Measurement System

The experimental setup, shown in Figure 4.2, comprised a microfluidic device, an inverted fluorescence microscope (DMi8, Leica Microsystems, Wetzlar, Germany), and an sCMOS camera (Neo 5.5, Andor, Belfast, Northern Ireland). The outlet fluidic connection was made by inserting an 18-gauge, 90º syringe needle tip into the pre-cored outlet port. FFP and thrombin solutions were withdrawn through the channel by a syringe pump (KDS Legato 111, KD Scientific, Holliston, Massachusetts, USA), which was connected to the single outlet of the microchannel.

A three-way valve at the outlet provided the option of withdrawing fluid through the channel with a manual syringe. PBS was first withdrawn into the channel with a manual syringe, and flow to the syringe pump was shut off by the three-way valve. After ensuring that the channel had been filled without any trapped air bubbles or debris, the manual syringe was disengaged to allow pressures at the inlets and outlet to be at an equilibrium. The three-way valve was then manipulated to enable automatic fluid withdrawal by the syringe pump, closing off the fluidic connection to the manual syringe. The syringe pump was placed at the same height as the microscope stage to avoid any backflow induced by any difference in static heights between the inlets and the outlet.

Imaging of fluorescently labeled fibrin formation during coagulation was achieved through the camera which was connected to the inverted fluorescence microscope. Image analysis was conducted on the acquired images as a means of characterizing the clots. Image analysis methods and clot characterization are discussed in Section 4.3.

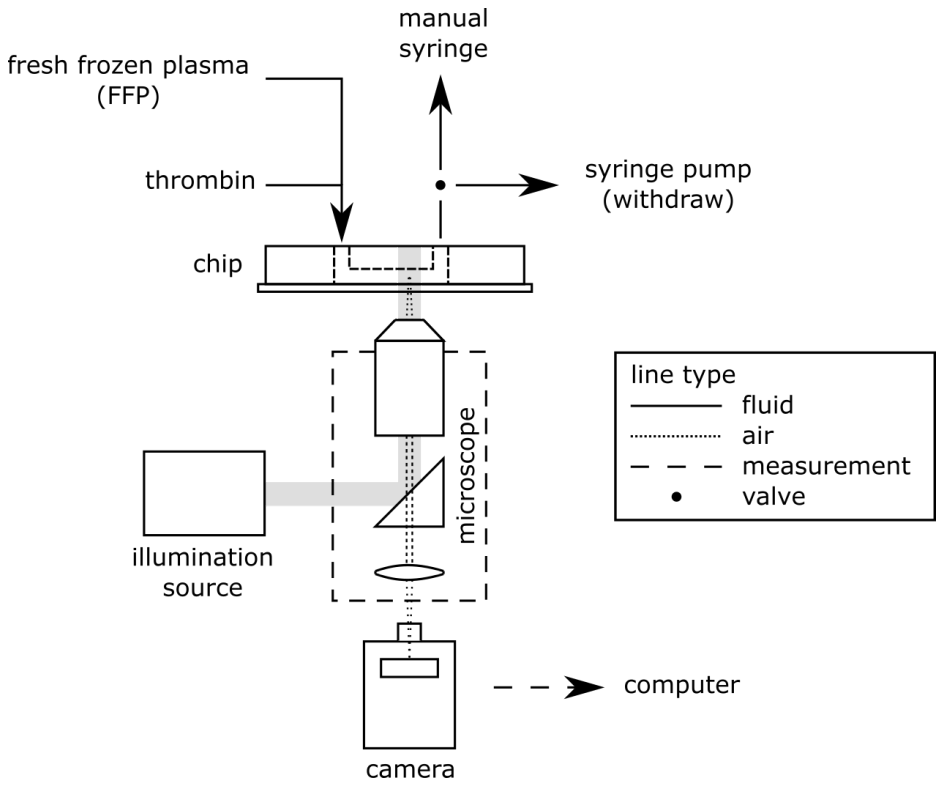

Figure 4.2 Flow testing apparatus.

4.2.4 Sources of Uncertainty

During each experimental run, flow instability is the main source of uncertainty. One of the causes of this instability has been observed to be induced by unbalanced inlet conditions. Flow instability here refers to oscillating movement of the boundary between the two flow streams. Reagents in the inlet wells formed droplets at the top of the wells. Differing droplet radii and static heights would cause unbalanced inlet pressures. The distinct densities of each inlet reagent would cause the droplets at the inlets to diminish at different rates, further causing unbalance of inlet driving forces between the two streams.

Flow stability could also be hindered by compliance within the system as a result of flexible tubing, flexible PDMS channel walls, and air bubbles on the order of 100 μm in diameter within the system [61]. In this instance, flow instability is concerned with varying flow rates within a particular experimental run. Often, protein clusters emerged within the FFP fluid stream, contributing to unwanted obstructions within the microchannel. At the onset of clotting, it was also likely that the flow rate had not stabilized to be at the desired flow rate.

Variation in channel dimensions caused by fabrication deviations and PDMS deformability would have effects on the flow rate. Hence, the initial shear rate at the co-flow stream boundaries would be affected by deviations in microchannel dimensions. Any height difference between the microchannel device and syringe pump would similarly affect the flow rate. A less significant source of flow rate uncertainty was from the syringe pump with a known accuracy of ± 0.5%.

To avoid unregulated clotting at transient flow rates, priming was initiated with PBS. This initial step, however, introduced uncertainties in the reagent concentrations caused by dilution of FFP and thrombin in PBS. Table 4.1 provides the estimated values for some of the mentioned sources of experimental uncertainty.

Table 4.1 Sources of Experimental Uncertainty

Source	Nominal	Uncertainty	Notes
FFP concentration	1.025 g/mL	− 0.2 g/mL	Caused by PBS dilution
Thrombin concentration	12.5 U/mL	− 2.5 U/mL	Caused by PBS dilution
Microchannel height	12 μm	± 1 μm	Caused by fabrication deviations and PDMS deformability
Microchannel width	300 μm	±10 μm	Caused by fabrication deviations and PDMS deformability
Syringe pump	100 nL/min	± 0.5 nL/min	Caused by pump accuracy
	200 nL/min	± 1.0 nL/min	
	400 nL/min	± 2.0 nL/min	

4.3 Image Acquisition and Analysis

The monitoring of clot formation was conducted via fluorescent images of clots acquired at one-minute intervals for a duration of 20 min, using the microscope interface software (LAS X, Leica Microsystems, Buffalo Grove, Illinois, USA). Higher fluorescence intensities indicate that a greater extent of crosslinking had occurred, hence predicting a higher density of fibrin. All clot images were taken with exposure of 300 ms. Brightfield images were obtained concurrently with fluorescent images of the fibrin clot to assist with locating corresponding channel regions and walls. Once coagulation was achieved within the channel, clot evolution was examined by stained fibrin microscope images.

The field of view for the observation region is shown by the 415.84 μm × 350.84 μm brightfield image in Figure 4.3, which was taken close to the inlet junction. All intensity profile measurements were made 300 μm downstream from where the two streams first meet, as indicated by the bold red line. Fluorescence intensities were extracted along this

profile and analyzed using MATLAB (The MathWorks, Inc., Natick, Massachusetts, USA).

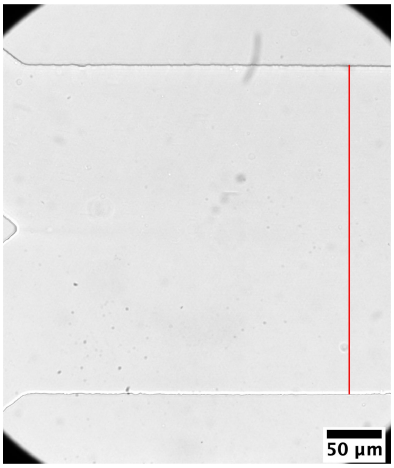

Figure 4.3 Brightfield image of clot formation observation region in microchannel.

4.3.1 Measurement of Clot Density

Higher fluorescence intensities were correlated with higher fibrin densities within the fibrin clot. Fluorescence has been observed to be difficult to calibrate, with fibrin fluorescence varying up to ±50% coefficient of variation across human donors [22]. Therefore, intensity measurements were normalized by the maximum intensity measured within each experimental run. Furthermore, normalized intensity values account for any concentration discrepancies of Alexa Fluor 594-conjugated fibrinogen between runs, caused by dilution from residue priming saline. The initial FFP stream was observed to exhibit low-level fluorescence intensities, therefore, intensity measurements were calibrated by removing this initial fluorescence measured at time 0 min. Uncalibrated and calibrated normalized intensity measurements at 0 min, 10 min and 20 min for 100

nL/min flow rate are shown in Figure 4.4. The time-tracking of maximum normalized intensities provided a way to monitor clot growth.

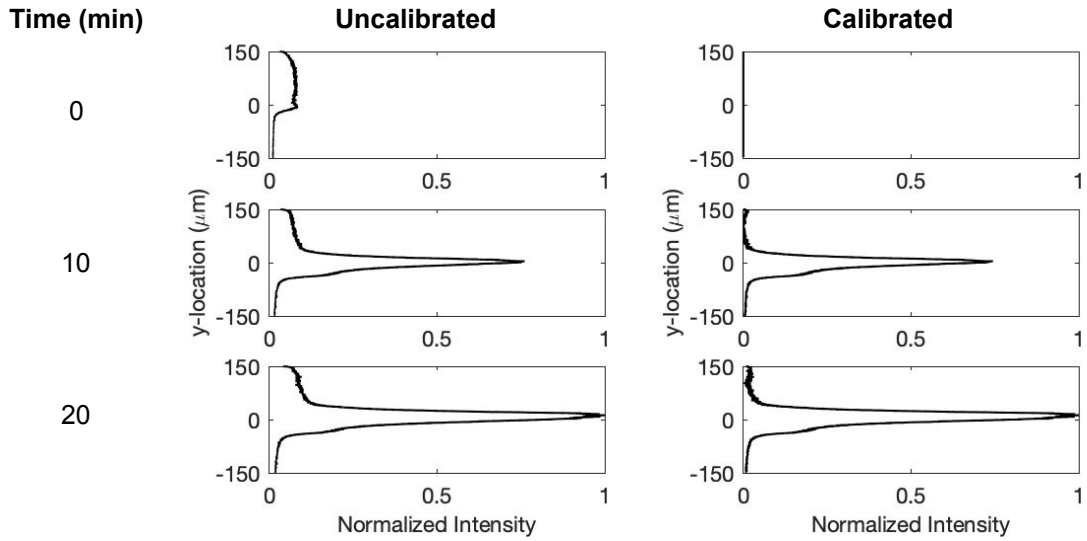

Figure 4.4 Uncalibrated and calibrated normalized intensities at 100 nL/min flow rate.

4.3.2 Measurement of Clot Shape and Distribution

Clot shape was determined by the analysis of calibrated and normalized intensity measurements at the base of the triangle measured at full-width, quarter-maximum (FWQM) region of the intensity graphs [70]. For this analysis, the *y*-axis of the intensity graphs were similarly normalized. As shown in Figure 4.5, a triangle was traced on the FWQM region of the graph, and angles θ_1, θ_2, and θ_3 were determined accordingly. Equations (4.1) and (4.2) were used to characterize clot asymmetry and acuteness, respectively from these three angles. An asymmetry value of one indicates perfect symmetry, while acuteness increases with decreasing θ_3 angle.

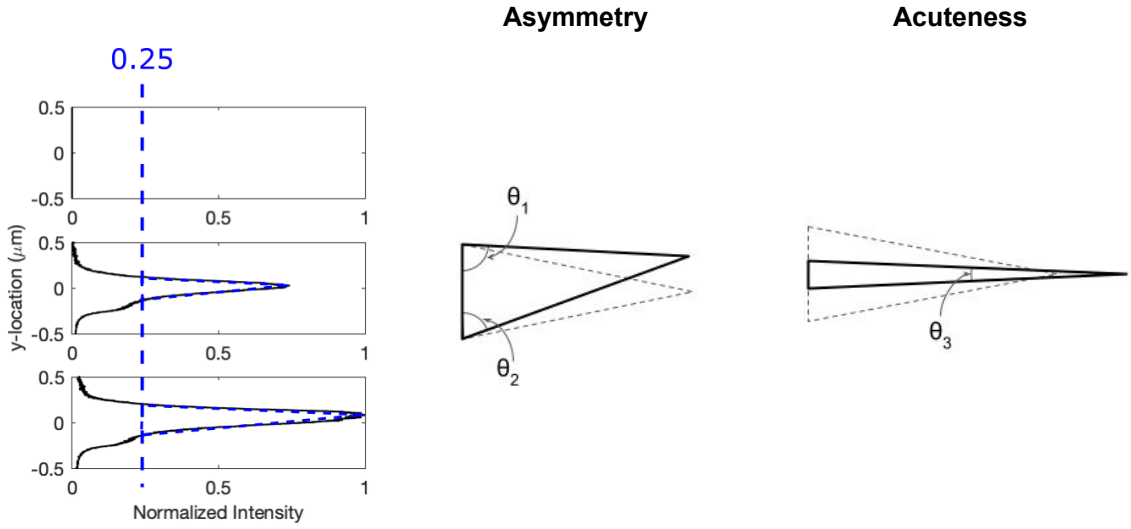

Figure 4.5 Clot shape analysis from intensity graphs.

$$\text{Asymmetry} = \frac{\text{minimum}[\theta_1, \theta_2]}{\text{maximum}[\theta_1, \theta_2]} \tag{4.1}$$

$$\text{Acuteness} = \theta_3 \tag{4.2}$$

Skewness and kurtosis were used to describe the clot density distribution in the FWQM region. In order to investigate the effect of a coagulation inhibitor on the formation of RBC aggregates, a similar time-tracking of skewness and kurtosis has been performed, in search of temporal changes in ultrasound echo amplitudes [71]. This approach has likewise been used to measure biofuel blending at the interface between two distinct fluids in a microfluidic viscometer that had a similar Y-channel configuration [72].

In this work, skewness, *S* and kurtosis, *K* for *n* values of a variable *x* were computed according to the implementation in MATLAB, as shown in equations (4.3) and (4.4), respectively. In this case, the variable *x* refers to the normalized clot intensity

measurements. It is noted that an alternative definition of kurtosis subtracts 3 from this kurtosis formula, such that a normal distribution would have a value of $K = 0$.

$$S = \frac{\frac{1}{n}\sum_{i=1}^{n}\left(x_i - \bar{x}\right)^3}{\left[\sqrt{\frac{1}{n}\sum_{i=1}^{n}\left(x_i - \bar{x}\right)^2}\right]^3} \tag{4.3}$$

$$K = \frac{\frac{1}{n}\sum_{i=1}^{n}\left(x_i - \bar{x}\right)^4}{\left[\frac{1}{n}\sum_{i=1}^{n}\left(x_i - \bar{x}\right)^2\right]^2} \tag{4.4}$$

$S = 0$ corresponds to a symmetrical probability distribution, while positive values of skewness refer to the mean and median of the clot density distribution being greater than the mode of the distribution. Negative values of skewness correspond to the mean and median being of lesser value than the mode.

$K = 3$ corresponds to a probability distribution having a kurtosis that is similar to a normal distribution. For $K > 3$, the distribution has longer tails in comparison with a normal distribution, while for $K < 3$, the tails are shorter.

5. RESULTS AND DISCUSSION

The major results for clot analogs formation between co-flow fluid streams are presented in this section. Clot formation was confirmed by fluorescence imaging of fibrin. Clot density shape and density distribution characterization was achieved through image analysis of the clots captured at one-minute intervals over a period of 20 min.

5.1 Clot Density

Figures 5.1, 5.2 and 5.3 present a condensed quantity of intensity images acquired at 10 min intervals, and the corresponding normalized fluorescence intensities measured across the channel width at x = 300 μm (downstream of inlet junction). Two experimental runs were conducted for each withdrawal flow rate of 100 nL/min, 200 nL/min, and 400 nL/min. The full range of fluorescence images taken at 1 min intervals and corresponding intensity graphs are presented in Appendix A.

In addition to the primary peak in the fluorescence signal intensity, satellite peaks are occasionally observed. A plausible explanation is that these satellite peaks are attributed to changes in inlet pressure conditions due to unstable and unbalanced inlet conditions, as discussed in Section 4.2.4. This instability results in a moving boundary between the co-flow streams causing the continued formation of the clot to relocate in the y-direction. Another possible cause for extra peaks is the change in FFP stream density, as the initial priming fluid (i.e., PBS) is displaced by FFP, causing a lateral shift in the location where clot formation occurs. High intensity spots or clusters visible in the fluorescence images correspond to protein clusters found in FFP. Run 2 of flow rate 100 nL/min, Run 1 of

flow rate 200 nL/min, and Run 2 of flow rate 400 nL/min contained more protein clusters, as seen in Figures 5.1, 5.2, and 5.3. Since intensity measurements are only analyzed at x = 300 μm, the effects of these protein clusters are most visible in the intensity graphs of Run 2 of flow rate 400 nL/min (Figure 5.3). Within the field-of-view of the camera for Run 2 of flow rate 400 nL/min, protein clusters are visible throughout the top half of the channel, causing the corresponding intensity graphs to have multiple peaks. It is observed that these protein clusters obstruct flow within the FFP stream, pushing the clot to form in the lower section of the channel (negative y-direction).

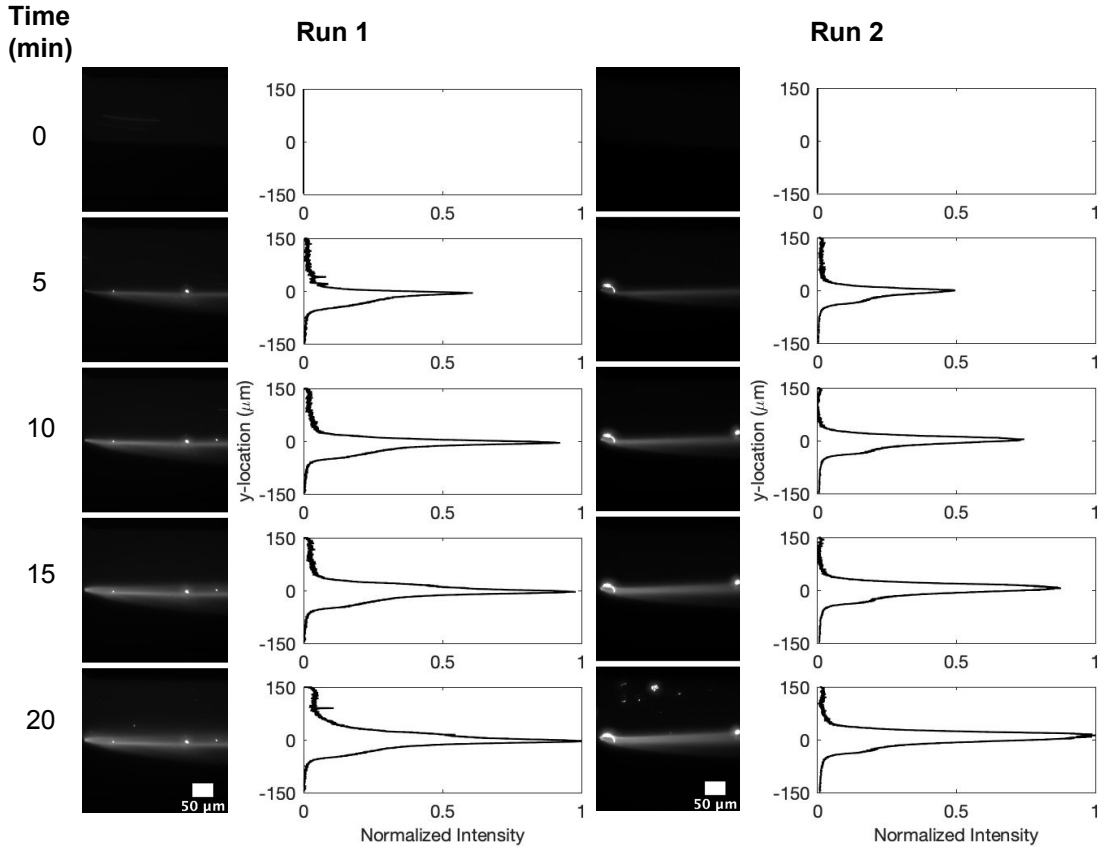

Figure 5.1 Clot intensities at 100 nL/min.

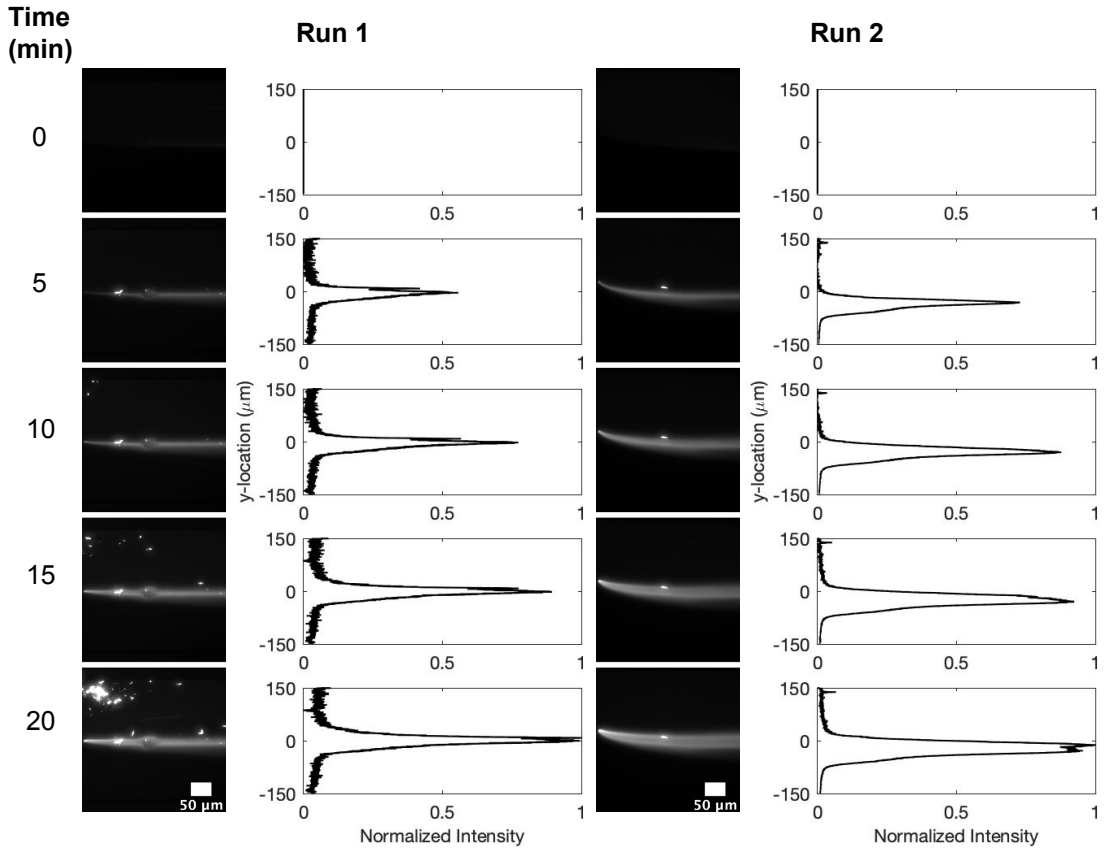

Figure 5.2 Clot intensities at 200 nL/min.

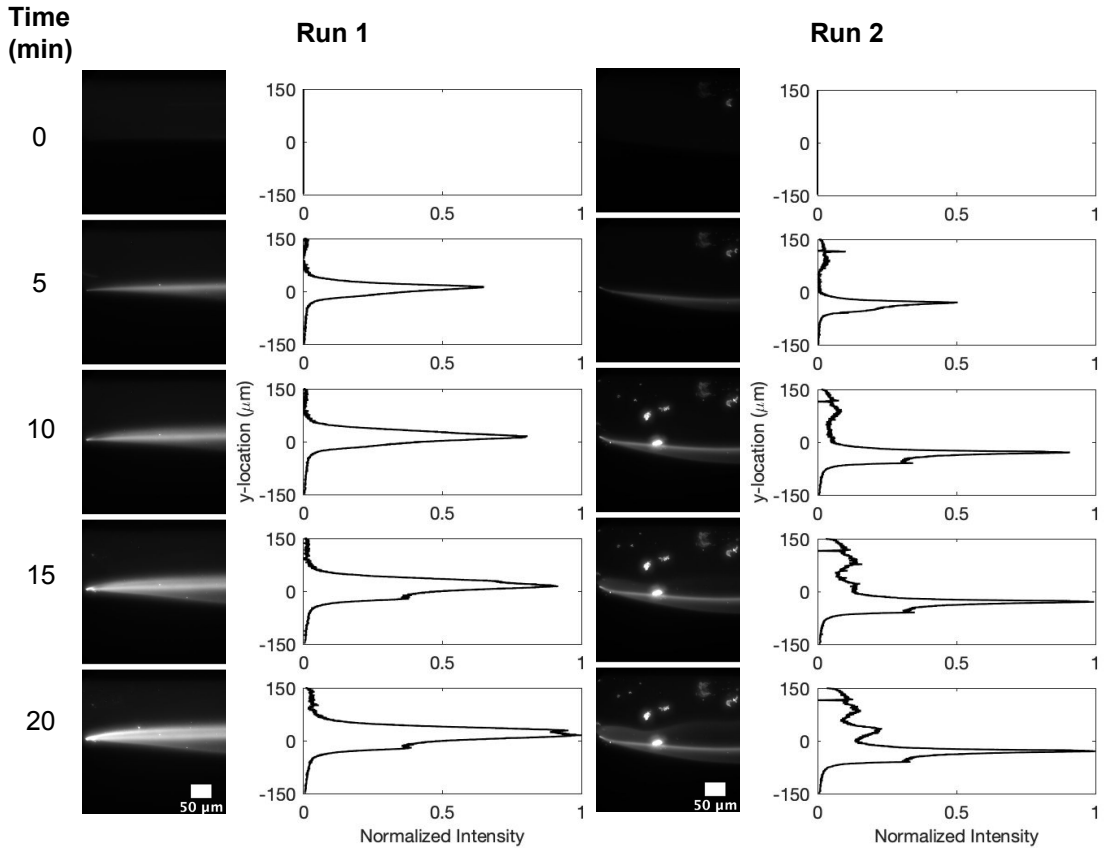

Figure 5.3 Clot intensities at 400 nL/min.

The time progression of normalized maximum intensities for each experimental run is shown in Figure 5.4. Exponential curve fits using equation (5.1) were conducted on each experimental run. The first-order exponential time constants, τ were extracted from these curve fits and presented in Table 5.1.

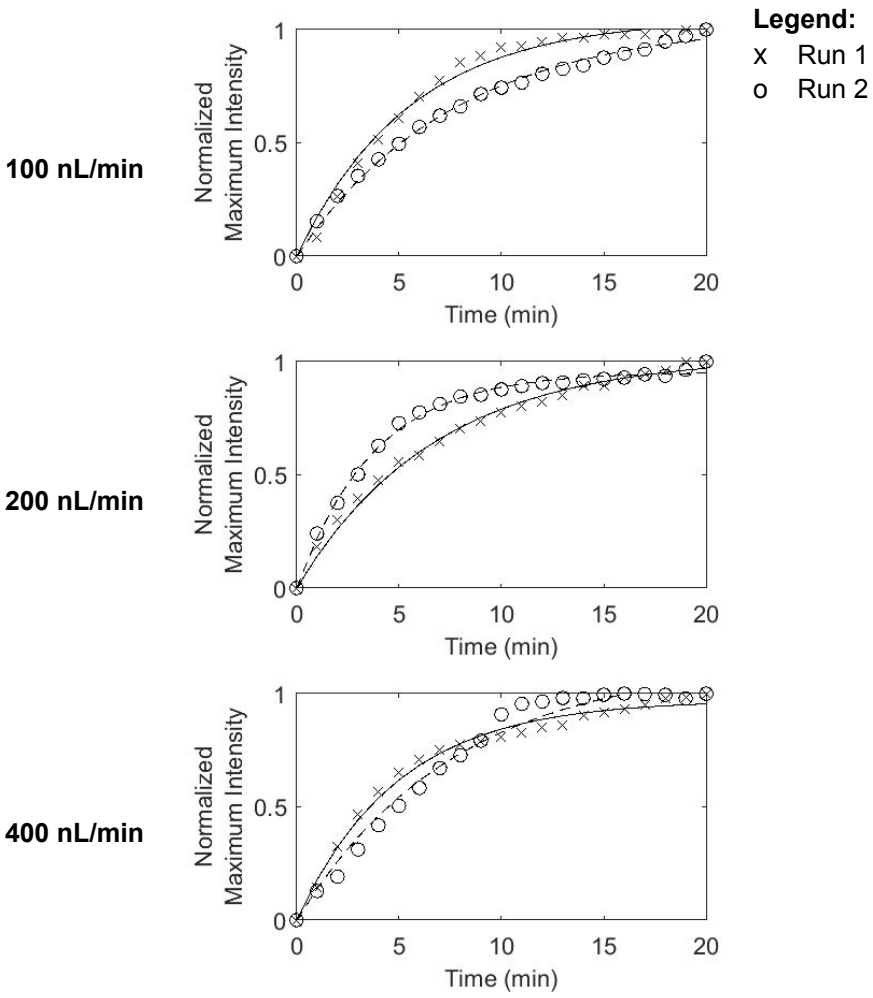

Figure 5.4 Time progression of normalized maximum intensities.

$$y = c(1 - e^{-\frac{t}{\tau}}) \tag{5.1}$$

Table 5.1 First-Order Time Constants from Exponential Curve Fit

Flow Rate (nL/min)	Run	Time Constant, τ (min)		
		Value	Average	Difference
100	1	5.53	6.62	2.19
	2	7.72		
200	1	6.77	5.23	3.01
	2	3.76		
400	1	4.93	6.34	2.82
	2	7.74		

Based on the time constants presented in Table 5.1, there is a difference of around 3 min between replicate runs. For all three flow rates, there is at least one run with visibly more protein clusters, as shown by the high intensity patches in Run 2 of Figure 5.1, Run 1 of Figure 5.2, and Run 2 of Figure 5.3. The higher time constants in Table 5.1 seem to correspond with the appearance of these protein clusters. Nevertheless, the time constant averages for each flow rate show a lack of contrast, with a time constant total average of around 6 min. This suggests that clot growth rate is consistent across the different flow rates between 100 nL/min and 400 nL/min.

5.2 Clot Shape and Density Distribution

The time progression of clot asymmetry and acuteness obtained from the FWQM region of the intensity graphs are presented in Figure 5.5. Connecting line segments in Figure 5.5 are for visual tracing and not presented as a model fit. Table 5.2 reports the final recorded asymmetry and acuteness measurements at the end of each experimental run at 20 min.

The formed clots are mostly symmetrical, with asymmetry values being close to one. This result conveys that clot growth rate in the opposite y-directions across the co-flow boundary is close to being equal. With decreasing peak angles in the intensity graphs, acuteness of the clot increases with time. The experimental runs containing more protein clusters appear to have clots with higher acuteness at 20 min, which is probably a consequence of the protein clusters restricting clot growth in the lateral direction of the channel. Nonetheless, the final asymmetry and acuteness replicate averages at 20 min

show that the final clot shape across the width of the channel is not influenced by the withdrawal flow rate. The time progression of asymmetry values appears steady throughout each experimental run, with asymmetry values between 0.9 and 1.0. Acuteness, however, only achieves steady state (roughly 10% of the steady-state value) after 15 min.

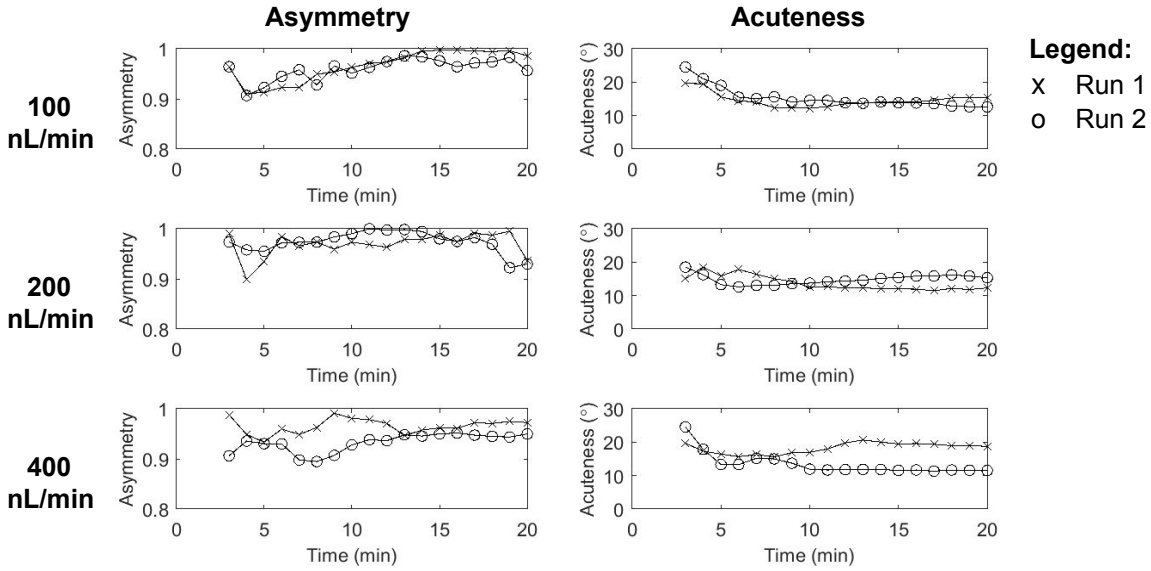

Figure 5.5 Time progression of asymmetry and acuteness.

Table 5.2 Asymmetry and Acuteness at 20 Minutes

Flow Rate (nL/min)	Run	Asymmetry			Acuteness (°)		
		Value	Average	Difference	Value	Average	Difference
100	1	0.986	0.971	0.029	15.34	13.98	2.70
	2	0.957			12.63		
200	1	0.936	0.933	0.007	12.29	13.81	3.04
	2	0.930			15.33		
400	1	0.972	0.961	0.023	18.69	15.11	7.16
	2	0.950			11.53		

Skewness and kurtosis were used to describe the fluorescence intensity distribution as a function of time. Similar to clot asymmetry and acuteness analyses, skewness and kurtosis were determined for the datasets within the FWQM region of the intensity measurements. Figure 5.6 presents the time evolution in skewness and kurtosis of clot density distribution. Again, the connecting line segments in Figure 5.6 are for visual tracing and not presented as a model fit. Table 5.3 reports the final recorded skewness and kurtosis values at the end of each experimental run at 20 min.

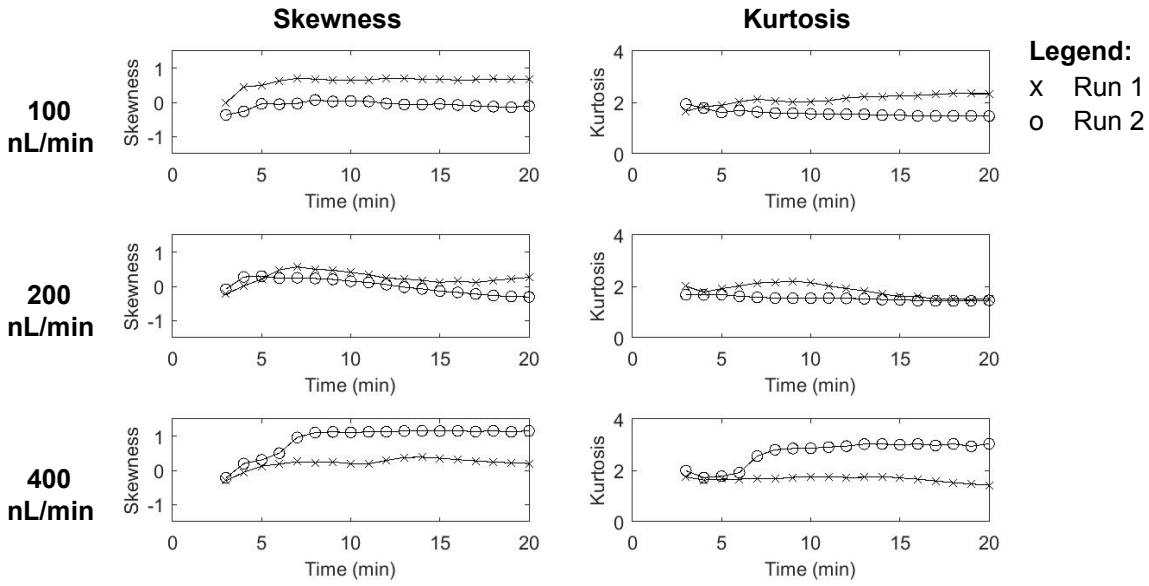

Figure 5.6 Time progression of skewness and kurtosis.

Table 5.3 Skewness and Kurtosis at 20 Minutes

Flow Rate (nL/min)	Run	Skewness			Kurtosis		
		Value	Average	Difference	Value	Average	Difference
100	1	0.678	0.288	0.782	2.338	1.900	0.876
	2	-0.103			1.463		
200	1	0.265	0.022	0.573	1.520	1.488	0.063
	2	-0.308			1.456		
400	1	0.200	0.678	0.955	1.421	2.229	1.616
	2	1.155			3.037		

At 20 min, the skewness values for most experimental runs (except for Run 1 of 100 nL/min and Run 2 of 400 nL/min) trend toward zero value of skewness (between -0.5 and 0.5 skewness), indicating that the fibrin density distribution is close to a symmetrical distribution. The fibrin density distribution of Run 1 of 100 nL/min and Run 2 of 400 nL/min at 20 min, however, are positively skewed at 0.678 and 1.155, respectively.

At 20 min, only Run 2 of 400 nL/min has a kurtosis value that is close to 3, meaning that the kurtosis of the distribution is similar to the kurtosis of a normal distribution. The remaining experimental runs have $K < 3$, meaning that the distribution has shorter tails, with fewer and less extreme outliers than a normal distribution.

Skewness and kurtosis reach an approximately constant level after approximately 10 min. In the first few minutes after introduction of thrombin, the fibrin network structure begins to develop. However, after approximately 10 min, the clot attains a stable density distribution.

5.3 Flow Stability

Flow stability experiments were conducted with water being introduced at both inlets. Food dye was added to one stream to assist with the visualization of the co-flow boundary. Since both streams have identical fluid properties, it is expected for the co-flow boundary to be precisely in the middle of the microchannel, in the *y*-direction. Figure 5.7 presents images taken at 1 min intervals at withdrawal flow rate of 100 nL/min. Numbering within the images presents the sequence at which the images were taken. These images demonstrate that flow was reasonably stable. This technique was

used to adjust the experimental methodology accordingly, to assist with the control of flow stability.

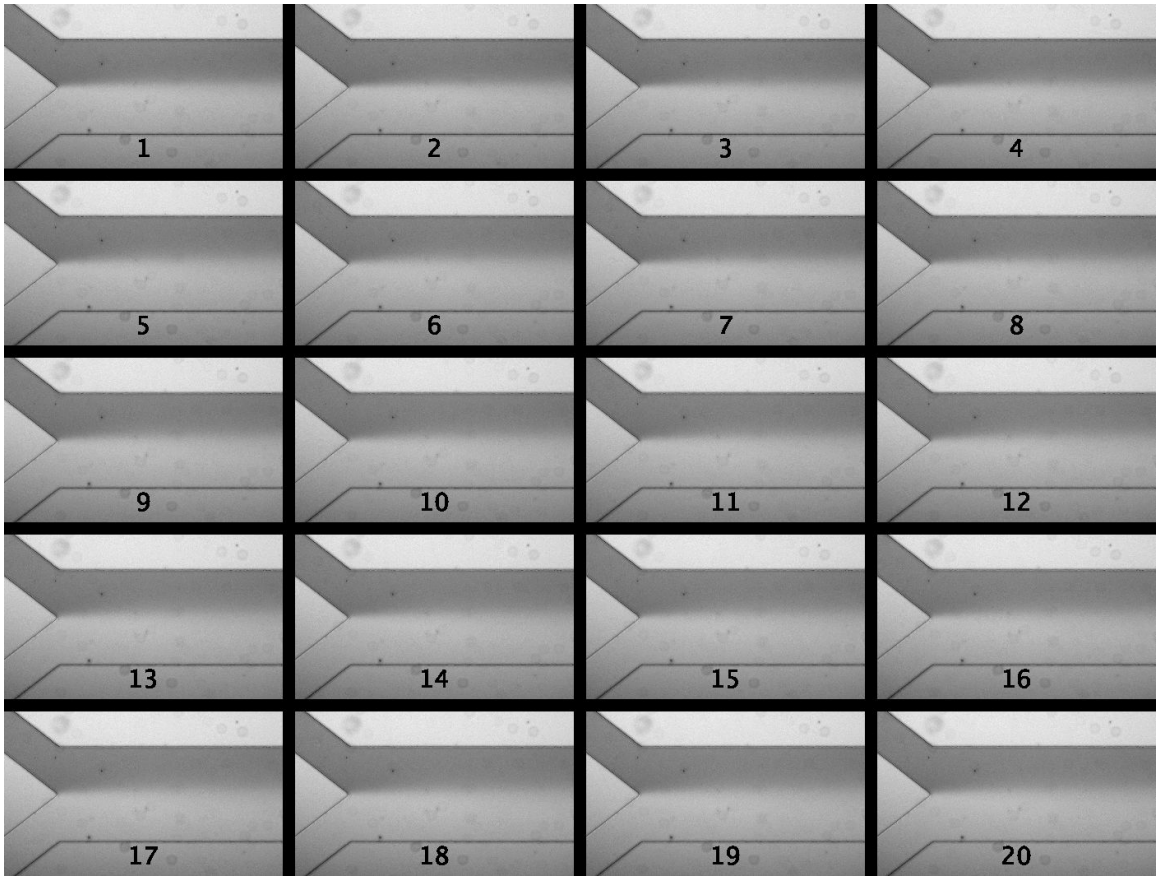

Figure 5.7 Monitoring flow stability at the co-flow boundary, at 1 min intervals.

5.4 Uncertainty Analysis

Surface profiler (Wyko NT9100, Bruker Corp., Tucson, AZ) measurements conducted on multiple microchannel devices are shown in Table 5.4. Microchannel cross-sectional height measurements show a standard deviation of 0.11 μm, while width measurements have a standard deviation of 5.67 μm. These channel dimensions would alter the velocity profile within the channel, as shown in equation (3.1). These deviations

ultimately affect the accuracy of the estimated initial co-flow shear rates presented in Section 3.2. Nevertheless, since clot growth rate, shape and distribution seem to be independent of initial shear rate for the flow rate range of 100 nL/min to 400 nL/min, these channel dimensional deviations are deemed to be acceptable.

Table 5.4 Surface Profiler Measurements of Microchannel Dimensions

Measurement	**Height (μm)**	**Width (μm)**
1	11.54	305.56
2	11.71	312.74
3	11.89	308.90
4	11.76	299.37
5	11.83	-
6	11.82	-
7	11.83	-
8	11.73	-
Standard Deviation	**0.11**	**5.67**

6. CONCLUSIONS

A microfluidic device capable of fabricating fibrin clots between co-flow fluid streams at physiological initial shear rates of 22.6 s^{-1}, 45.2 s^{-1}, and 90.4 s^{-1} was developed. Fibrin clots were formed and imaged using fluorescence labeling of FFP paired with fluorescence microscopy. Image analysis was used to quantify fibrin density, which was highest where the FFP and thrombin streams initially met. Shape parameters were developed, namely asymmetry and acuteness, to describe the shape of the clot in the FWQM region of the intensity plot. Skewness and kurtosis were used to describe the density distribution within the clot in the FWQM region.

Progression of intensities exhibited similar time constants across flow rates from 100 nL/min to 400 nL/min. From the clot shape and clot density distribution parameters, it was observed that steady state was achieved within 15 min of each experimental run. Formed clots exhibited similar growth rate, shape and distribution characteristics, independent of flow rate and initial shear rate.

Distinct withdrawal flow rates dictated the initial shear rates at the co-flow boundary (Figure 3.4) at which clotting was initiated. However, as clot size increased, shear rates increased accordingly at the surface of the clot. From simulated pressure results (Figure 3.5), it was predicted that the pressure difference across the clot for the different flow rates were similar. Clot permeability has been shown to be a function of fibrinogen concentration [33], and since the same concentrations of FFP and thrombin were used for all experiments, it is proposed that clots formed in all six experiments had similar

permeability values. The results presented in Section 5 support the hypothesis that clot shape and density distribution are insensitive to initial co-flow shear rate. Pressure difference across the clot and clot permeability are predicted to be the dominant factors of clot growth, shape, and density distribution.

Future work would involve altering substance concentration, design parameters (e.g., channel dimensions), substance combinations (e.g., whole blood and different clotting factors), and operating conditions (e.g., pressure difference across clot and relative flow rates) to engineer clot analogs with distinguishable shapes and density distributions. Clinical specimens can be examined for blood clot composition and heterogeneity, assisting with customizing the engineered device to manufacture accurate clot analogs. Better control of initial co-flow shear rate and pressure difference across the clot can be achieved pneumatically at the inlets by modifying the hydraulic resistance of inlet feeders within the microfluidic device [73]. Flow control could also be improved by exploring other flow infusion or gravity feed methods.

REFERENCES CITED

[1] S. Duffy *et al.*, "Novel methodology to replicate clot analogs with diverse composition in acute ischemic stroke," *J. Neurointerv. Surg.*, vol. 9, no. 5, pp. 486–491, May 2017.

[2] S. L. Diamond, "Systems analysis of thrombus formation," *Circ. Res.*, vol. 118, no. 9, pp. 1348–1362, Apr. 2016.

[3] N. K. R. Pandian, R. G. Mannino, W. A. Lam, and A. Jain, "Thrombosis-on-a-chip: Prospective impact of microphysiological models of vascular thrombosis," *Current Opinion in Biomedical Engineering*, vol. 5, pp. 29–34, Mar. 2018.

[4] C. N. Bagot and R. Arya, "Virchow and his triad: a question of attribution," *Br. J. Haematol.*, vol. 143, no. 2, pp. 180–190, Oct. 2008.

[5] T. Watson, E. Shantsila, and G. Y. H. Lip, "Mechanisms of thrombogenesis in atrial fibrillation: Virchow's triad revisited," *Lancet*, vol. 373, no. 9658, pp. 155–166, Jan. 2009.

[6] A. L. Kuharsky and A. L. Fogelson, "Surface-mediated control of blood coagulation: the role of binding site densities and platelet deposition," *Biophys. J.*, vol. 80, no. 3, pp. 1050–1074, Mar. 2001.

[7] U. M. Okorie, W. S. Denney, M. S. Chatterjee, K. B. Neeves, and S. L. Diamond, "Determination of surface tissue factor thresholds that trigger coagulation at venous and arterial shear rates: amplification of 100 fM circulating tissue factor requires flow," *Blood*, vol. 111, no. 7, pp. 3507–3513, Apr. 2008.

[8] J. W. Weisel, "Biophysics. Enigmas of blood clot elasticity," *Science*, vol. 320, no. 5875, pp. 456–457, Apr. 2008.

[9] N. Krasokha *et al.*, "Mechanical properties of blood clots - a new test method. Mechanische Eigenschaften von Thromben - Neue Untersuchungsmethoden," *Mat.-wiss. u. Werkstofftech.*, vol. 41, no. 12, pp. 1019–1024, Dec. 2010.

[10] J. W. Weisel, "Structure of fibrin: impact on clot stability," *J. Thromb. Haemost.*, vol. 5 Suppl 1, pp. 116–124, Jul. 2007.

[11] A. L. Fogelson and K. B. Neeves, "Fluid mechanics of blood clot formation," *Annu. Rev. Fluid Mech.*, vol. 47, pp. 377–403, Jan. 2015.

[12] B. Sebastian and P. S. Dittrich, "Microfluidics to mimic blood flow in health and disease," *Annu. Rev. Fluid Mech.*, vol. 50, no. 1, pp. 483–504, Jan. 2018.

[13] F. J. Tovar-Lopez *et al.*, "A microfluidics device to monitor platelet aggregation dynamics in response to strain rate micro-gradients in flowing blood," *Lab Chip*, vol. 10, no. 3, pp. 291–302, Feb. 2010.

[14] A. Jain, A. Graveline, A. Waterhouse, A. Vernet, R. Flaumenhaft, and D. E. Ingber, "A shear gradient-activated microfluidic device for automated monitoring of whole blood haemostasis and platelet function," *Nat. Commun.*, vol. 7, p. 10176, Jan. 2016.

[15] W. S. Nesbitt *et al.*, "A shear gradient-dependent platelet aggregation mechanism drives thrombus formation," *Nat. Med.*, vol. 15, no. 6, pp. 665–673, Jun. 2009.

[16] F. C. Roessler *et al.*, "Development of a new clot formation protocol for standardized in vitro investigations of sonothrombolysis," *J. Neurosci. Methods*, vol. 237, pp. 26–32, Nov. 2014.

[17] R. Akhtar, M. J. Sherratt, J. K. Cruickshank, and B. Derby, "Characterizing the elastic properties of tissues," *Mater. Today*, vol. 14, no. 3, pp. 96–105, Mar. 2011.

[18] D. H. Wang, M. Makaroun, M. W. Webster, and D. A. Vorp, "Mechanical properties and microstructure of intraluminal thrombus from abdominal aortic aneurysm," *J. Biomech. Eng.*, vol. 123, no. 6, pp. 536–539, Dec. 2001.

[19] J. Y. Chueh, A. K. Wakhloo, G. H. Hendricks, C. F. Silva, J. P. Weaver, and M. J. Gounis, "Mechanical characterization of thromboemboli in acute ischemic stroke and laboratory embolus analogs," *AJNR Am. J. Neuroradiol.*, vol. 32, no. 7, pp. 1237–1244, Aug. 2011.

[20] Z. Chen *et al.*, "Microclot array elastometry for integrated measurement of thrombus formation and clot biomechanics under fluid shear," *Nat. Commun.*, vol. 10, no. 1, p. 2051, May 2019.

[21] F. Shen, C. J. Kastrup, Y. Liu, and R. F. Ismagilov, "Threshold response of initiation of blood coagulation by tissue factor in patterned microfluidic capillaries is controlled by shear rate," *Arterioscler. Thromb. Vasc. Biol.*, vol. 28, no. 11, pp. 2035–2041, Nov. 2008.

[22] S. Zhu, J. Chen, and S. L. Diamond, "Establishing the transient mass balance of thrombosis," *Arterioscler. Thromb. Vasc. Biol.*, 2018.

[23] J. G. Santiago, S. T. Wereley, C. D. Meinhart, D. J. Beebe, and R. J. Adrian, "A particle image velocimetry system for microfluidics," *Exp. Fluids*, vol. 25, no. 4, pp. 316–319, Sep. 1998.

[24] M. G. Beckman, W. C. Hooper, S. E. Critchley, and T. L. Ortel, “Venous thromboembolism: a public health concern,” *Am. J. Prev. Med.*, vol. 38, no. 4 Suppl, pp. S495–501, Apr. 2010.

[25] S. Johnson, S. Duffy, G. Gunning, M. Gilvarry, J. P. McGarry, and P. E. McHugh, “Review of mechanical testing and modelling of thrombus material for vascular implant and device design,” *Ann. Biomed. Eng.*, vol. 45, no. 11, pp. 2494–2508, Nov. 2017.

[26] V. Govindarajan *et al.*, “Impact of tissue factor localization on blood clot structure and resistance under venous shear,” *Biophys. J.*, vol. 114, no. 4, pp. 978–991, Feb. 2018.

[27] V. Balasubramanian, E. Grabowski, A. Bini, and Y. Nemerson, “Platelets, circulating tissue factor, and fibrin colocalize in ex vivo thrombi: real-time fluorescence images of thrombus formation and propagation under defined flow conditions,” *Blood*, vol. 100, no. 8, pp. 2787–2792, Oct. 2002.

[28] K. B. Neeves, D. A. R. Illing, and S. L. Diamond, “Thrombin flux and wall shear rate regulate fibrin fiber deposition state during polymerization under flow,” *Biophys. J.*, vol. 100, no. 3, Supplement 1, p. 199a, Feb. 2011.

[29] T. V. Colace, R. W. Muthard, and S. L. Diamond, “Thrombus growth and embolism on tissue factor-bearing collagen surfaces under flow: role of thrombin with and without fibrin,” *Arterioscler. Thromb. Vasc. Biol.*, vol. 32, no. 6, pp. 1466–1476, Jun. 2012.

[30] K. B. Neeves *et al.*, “Microfluidic focal thrombosis model for measuring murine platelet deposition and stability: PAR4 signaling enhances shear-resistance of platelet aggregates,” *J. Thromb. Haemost.*, vol. 6, no. 12, pp. 2193–2201, Dec. 2008.

[31] J. P. Collet *et al.*, “Influence of fibrin network conformation and fibrin fiber diameter on fibrinolysis speed,” *Arterioscler. Thromb. Vasc. Biol.*, May 2000.

[32] D. Chen, J. Wang, P. Wang, Q. Guo, Z. Zhang, and J. Ma, “Real-time monitoring of human blood clotting using a lateral excited film bulk acoustic resonator,” *J. Micromech. Microeng.*, vol. 27, no. 4, p. 045013, Mar. 2017.

[33] A. R. Wufsus, N. E. Macera, and K. B. Neeves, “The hydraulic permeability of blood clots as a function of fibrin and platelet density,” *Biophys. J.*, vol. 104, no. 8, pp. 1812–1823, Apr. 2013.

[34] P. Allan, “Microheology of fibrin clots,” phd, University of Leeds, 2012.

[35] M. A. Kotlarchyk, E. L. Botvinick, and A. J. Putnam, "Characterization of hydrogel microstructure using laser tweezers particle tracking and confocal reflection imaging," *J. Phys. Condens. Matter*, vol. 22, no. 19, p. 194121, May 2010.

[36] N. E. Hudson *et al.*, "Stiffening of individual fibrin fibers equitably distributes strain and strengthens networks," *Biophys. J.*, vol. 98, no. 8, pp. 1632–1640, Apr. 2010.

[37] R. Zhao, T. Boudou, W.-G. Wang, C. S. Chen, and D. H. Reich, "Decoupling cell and matrix mechanics in engineered microtissues using magnetically actuated microcantilevers," *Adv. Mater.*, vol. 25, no. 12, pp. 1699–1705, Mar. 2013.

[38] C. J. Wolfram, G. W. Rubloff, and X. Luo, "Perspectives in flow-based microfluidic gradient generators for characterizing bacterial chemotaxis," *Biomicrofluidics*, vol. 10, no. 6, p. 061301, Nov. 2016.

[39] N. L. Jeon, S. K. W. Dertinger, D. T. Chiu, I. S. Choi, A. D. Stroock, and G. M. Whitesides, "Generation of solution and surface gradients using microfluidic systems," *Langmuir*, vol. 16, no. 22, pp. 8311–8316, Oct. 2000.

[40] S. K. W. Dertinger, D. T. Chiu, N. L. Jeon, and G. M. Whitesides, "Generation of gradients having complex shapes using microfluidic networks," *Anal. Chem.*, vol. 73, no. 6, pp. 1240–1246, Mar. 2001.

[41] D. Irimia, D. A. Geba, and M. Toner, "Universal microfluidic gradient generator," *Anal. Chem.*, vol. 78, no. 10, pp. 3472–3477, May 2006.

[42] J. Loessberg-Zahl, A. D. van der Meer, A. van den Berg, and J. C. T. Eijkel, "Flow focusing through gels as a tool to generate 3D concentration profiles in hydrogel-filled microfluidic chips," *Lab Chip*, vol. 19, no. 2, pp. 206–213, Jan. 2019.

[43] B. Ha, J. Park, G. Destgeer, J. H. Jung, and H. J. Sung, "Transfer of microparticles across laminar streams from non-Newtonian to Newtonian fluid," *Anal. Chem.*, vol. 88, no. 8, pp. 4205–4210, Apr. 2016.

[44] F. Tian *et al.*, "Microfluidic co-flow of Newtonian and viscoelastic fluids for high-resolution separation of microparticles," *Lab Chip*, vol. 17, no. 18, pp. 3078–3085, Sep. 2017.

[45] M. Rossi, C. Cierpka, R. Segura, and C. J. Kähler, "Volumetric reconstruction of the 3D boundary of stream tubes with general topology using tracer particles," *Meas. Sci. Technol.*, vol. 22, no. 10, p. 105405, Aug. 2011.

[46] R. W. Muthard and S. L. Diamond, "Rapid on-chip recalcification and drug dosing of citrated whole blood using microfluidic buffer sheath flow," *Biorheology*, vol. 51, no. 2–3, pp. 227–237, 2014.

[47] A. A. Onasoga-Jarvis, T. J. Puls, S. K. O'Brien, L. Kuang, H. J. Liang, and K. B. Neeves, "Thrombin generation and fibrin formation under flow on biomimetic tissue factor-rich surfaces," *J. Thromb. Haemost.*, vol. 12, no. 3, pp. 373–382, 2014.

[48] H. Mao, P. S. Cremer, and M. D. Manson, "A sensitive, versatile microfluidic assay for bacterial chemotaxis," *Proc. Natl. Acad. Sci. U. S. A.*, vol. 100, no. 9, pp. 5449–5454, Apr. 2003.

[49] C. Kim *et al.*, "Diffusion- and convection-based activation of Wnt/β-catenin signaling in a gradient generating microfluidic chip," *Lab Chip*, vol. 12, no. 24, pp. 5186–5194, Dec. 2012.

[50] R. Lima *et al.*, "In vitro blood flow in a rectangular PDMS microchannel: experimental observations using a confocal micro-PIV system," *Biomed. Microdevices*, vol. 10, no. 2, pp. 153–167, Apr. 2008.

[51] K. L. Pitts and M. Fenech, "An analytic study on the effect of alginate on the velocity profiles of blood in rectangular microchannels using microparticle image velocimetry," *PLoS One*, vol. 8, no. 8, p. e72909, Aug. 2013.

[52] R. Mehri, C. Mavriplis, and M. Fenech, "Red blood cell aggregates and their effect on non-Newtonian blood viscosity at low hematocrit in a two-fluid low shear rate microfluidic system," *PLoS One*, vol. 13, no. 7, p. e0199911, Jul. 2018.

[53] E. Yeom, Y. J. Kang, and S.-J. Lee, "Changes in velocity profile according to blood viscosity in a microchannel," *Biomicrofluidics*, vol. 8, no. 3, p. 034110, May 2014.

[54] H. Ha and S.-J. Lee, "Hemodynamic features and platelet aggregation in a stenosed microchannel," *Microvasc. Res.*, vol. 90, pp. 96–105, Nov. 2013.

[55] K. R. M, S. Bhattacharya, S. DasGupta, and S. Chakraborty, "Collective dynamics of red blood cells on an in vitro microfluidic platform," *Lab Chip*, vol. 18, no. 24, pp. 3939–3948, Dec. 2018.

[56] Y. Sugii, S. Nishio, and K. Okamoto, "Measurement of a velocity field in microvessels using a high resolution PIV technique," *Ann. N. Y. Acad. Sci.*, vol. 972, pp. 331–336, Oct. 2002.

[57] P. Vennemann *et al.*, "In vivo micro particle image velocimetry measurements of blood-plasma in the embryonic avian heart," *J. Biomech.*, vol. 39, no. 7, pp. 1191–1200, 2006.

[58] F. M. White, *Viscous Fluid Flow*, 3rd edition. McGraw-Hill Education, 2005.

[59] H. Bruus, *Theoretical Microfluidics*. 2008.

[60] S. Chien, S. Usami, H. M. Taylor, J. L. Lundberg, and M. I. Gregersen, “Effects of hematocrit and plasma proteins on human blood rheology at low shear rates,” *J. Appl. Physiol.*, vol. 21, no. 1, pp. 81–87, Jan. 1966.

[61] B. Kirby, *Micro- and Nanoscale Fluid Mechanics: Transport in Microfluidic Devices*. Cambridge University Press, 2010.

[62] R. J. Trudnowski and R. C. Rico, “Specific gravity of blood and plasma at 4 and 37 degrees C,” *Clin. Chem.*, vol. 20, no. 5, pp. 615–616, May 1974.

[63] “Recommendation for a selected method for the measurement of plasma viscosity. International Committee for Standardization in Haematology,” *J. Clin. Pathol.*, vol. 37, no. 10, pp. 1147–1152, Oct. 1984.

[64] M. Raffel, C. E. Willert, S. T. Wereley, and J. Kompenhans, *Particle Image Velocimetry: A Practical Guide*. 2007.

[65] C. D. Meinhart, S. T. Wereley, and J. G. Santiago, “PIV measurements of a microchannel flow,” *Exp. Fluids*, vol. 27, no. 5, pp. 414–419, Oct. 1999.

[66] C. S. Niman *et al.*, “Controlled microfluidic switching in arbitrary time-sequences with low drag,” *Lab Chip*, vol. 13, no. 12, pp. 2389–2396, Jun. 2013.

[67] X. Xu, Z. Li, and A. Nehorai, “Finite element simulations of hydrodynamic trapping in microfluidic particle-trap array systems,” *Biomicrofluidics*, vol. 7, no. 5, p. 54108, Sep. 2013.

[68] K. L. Pitts, R. Mehri, C. Mavriplis, and M. Fenech, “Micro-particle image velocimetry measurement of blood flow: validation and analysis of data pre-processing and processing methods,” *Meas. Sci. Technol.*, vol. 23, no. 10, p. 105302, Aug. 2012.

[69] D. C. Duffy, J. C. McDonald, O. J. A. Schueller, and G. M. Whitesides, “Rapid prototyping of microfluidic systems in poly(dimethylsiloxane),” *Anal. Chem.*, vol. 70, no. 23, pp. 4974–4984, 1998.

[70] M. Rahmani, M. M. Khani, Z. K. Koohpar, and P. Molik, “Discrimination and quantification of autofluorescence spectra of human lung cells,” *Laser Phys.*, vol. 26, no. 10, p. 105604, Aug. 2016.

[71] K.-H. Nam, E. Yeom, H. Ha, and S. J. Lee, “Simultaneous measurement of red blood cell aggregation and whole blood coagulation using high-frequency ultrasound,” *Ultrasound Med. Biol.*, vol. 38, no. 3, pp. 468–475, Mar. 2012.

[72] S. Goel, P. S. Venkateswaran, R. Prajesh, and A. Agarwal, “Rapid and automated measurement of biofuel blending using a microfluidic viscometer,” *Fuel*, vol. 139, pp. 213–219, Jan. 2015.

[73] F. J. Tovar-Lopez *et al.*, “An investigation on platelet transport during thrombus formation at micro-scale stenosis,” *PLoS One*, vol. 8, no. 10, p. e74123, Oct. 2013.

APPENDIX A: RAW EXPERIMENTAL IMAGES AND INTENSITY GRAPHS

100 nL/min - Run 1

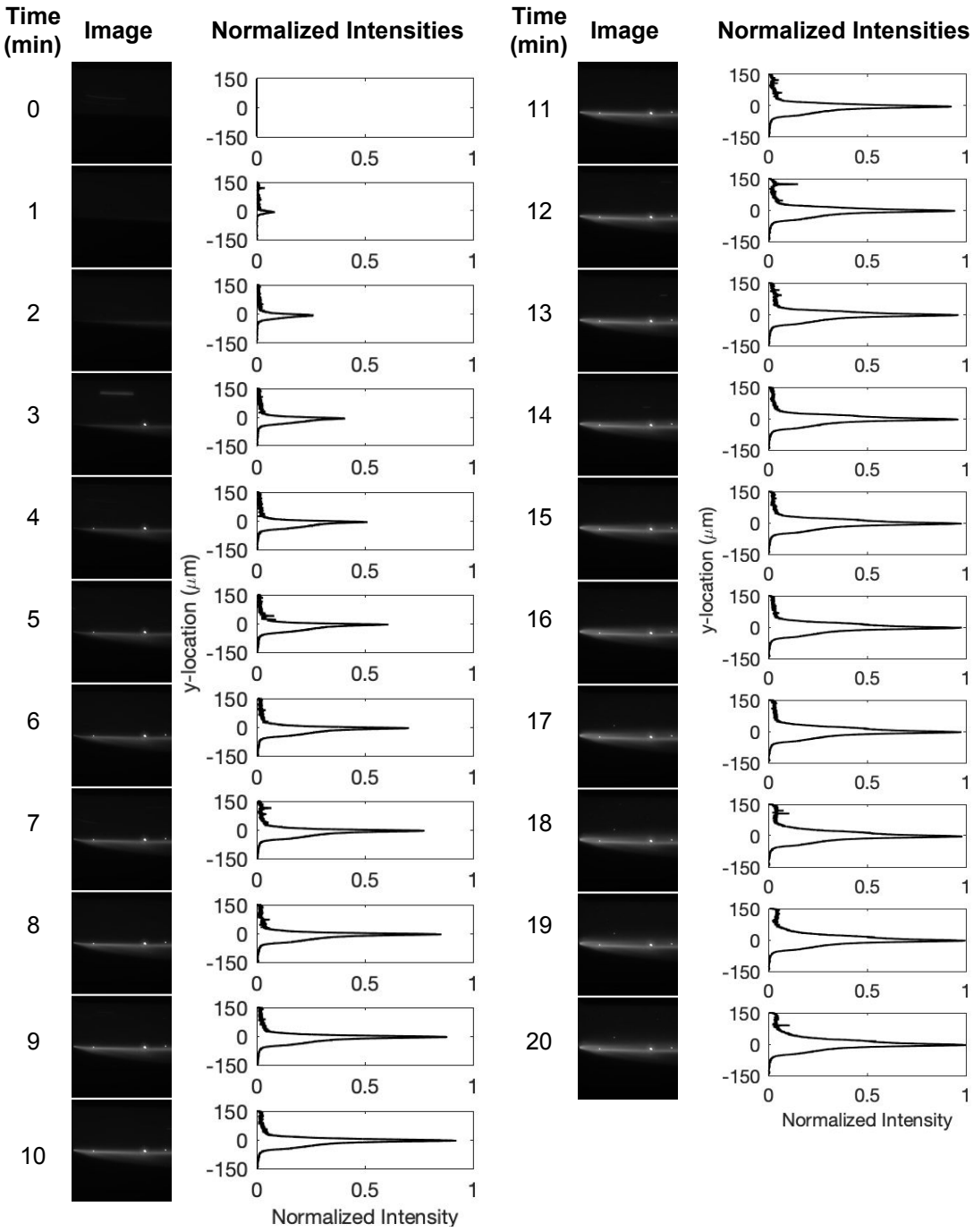

100 nL/min - Run 2

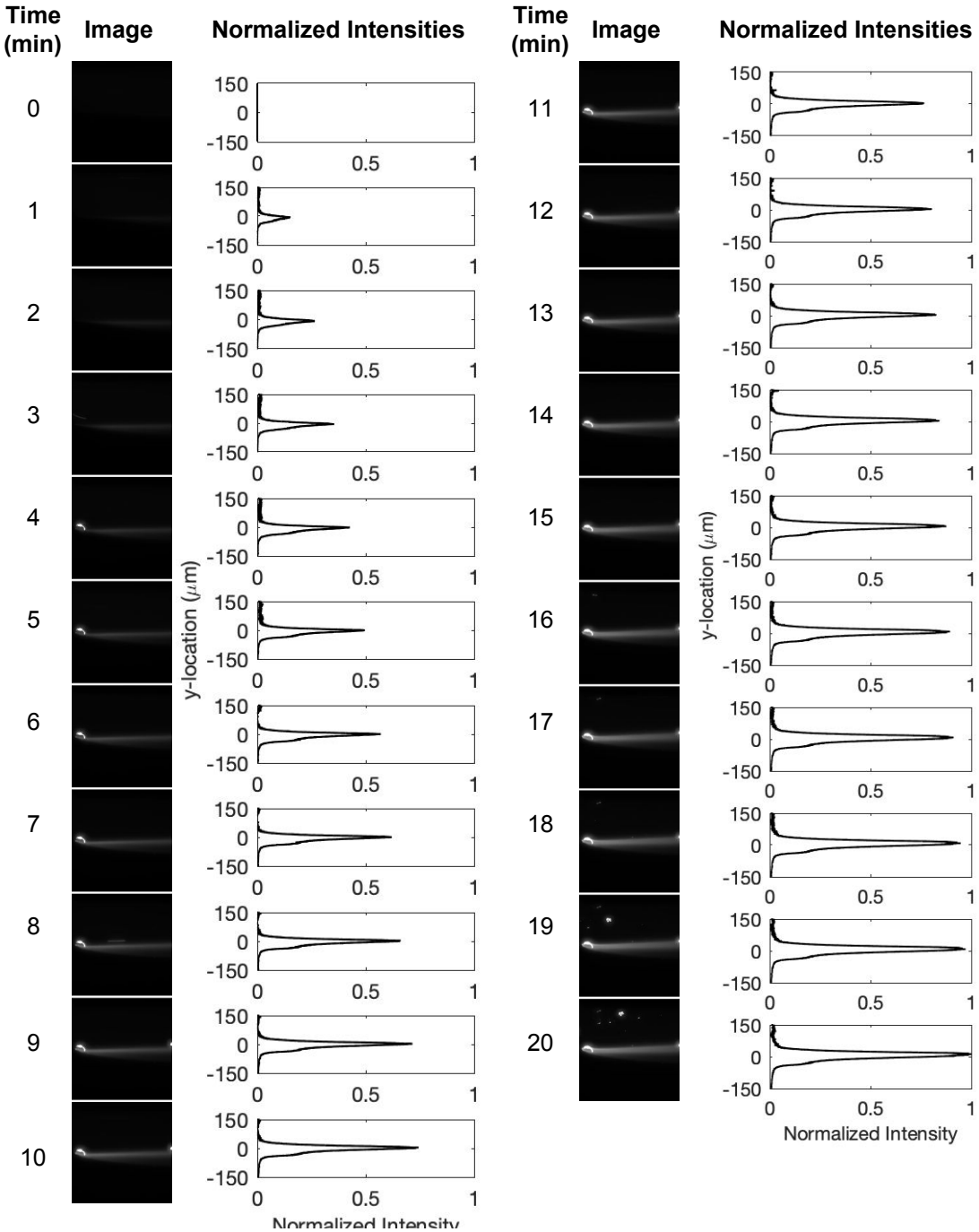

200 nL/min - Run 1

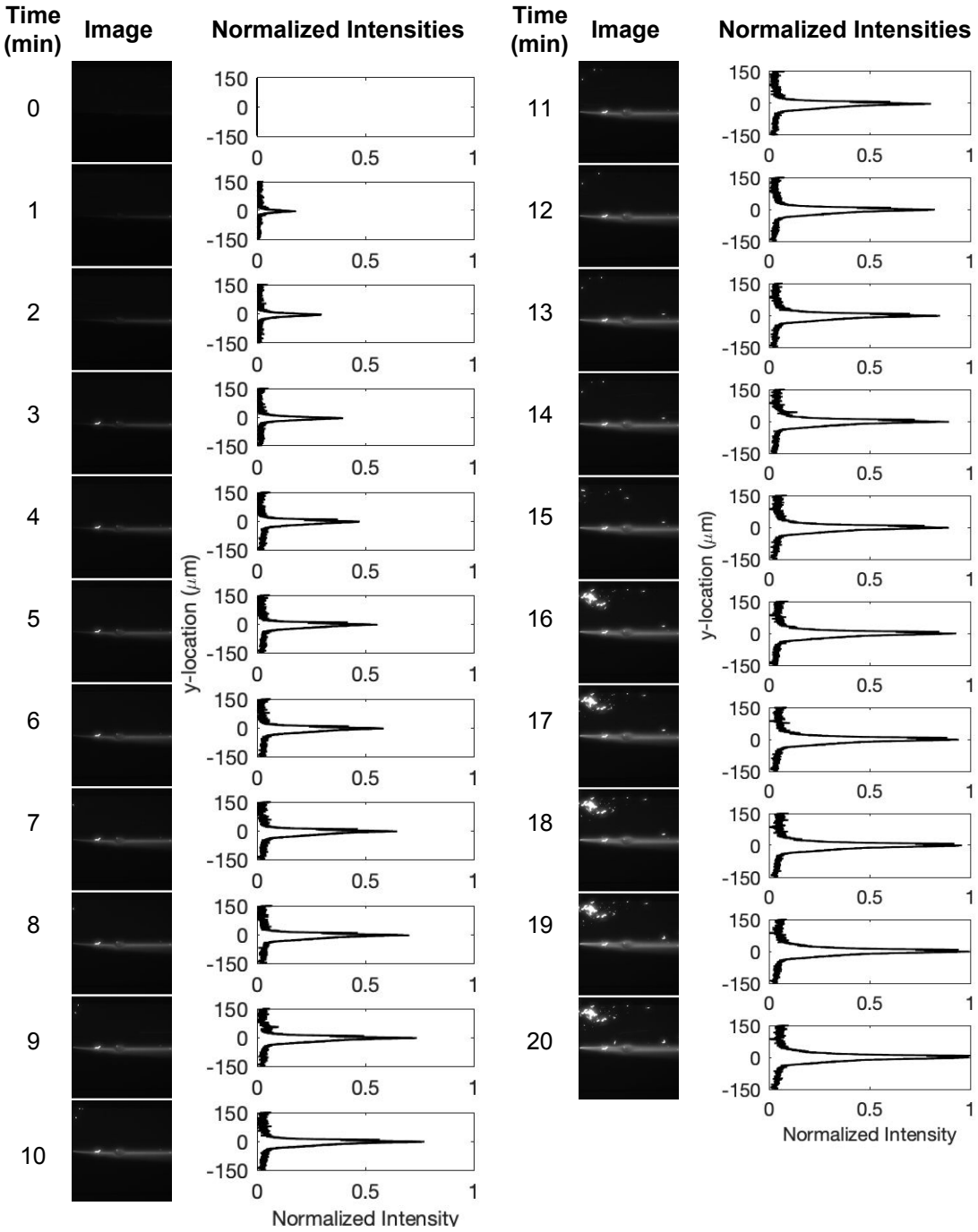

200 nL/min - Run 2

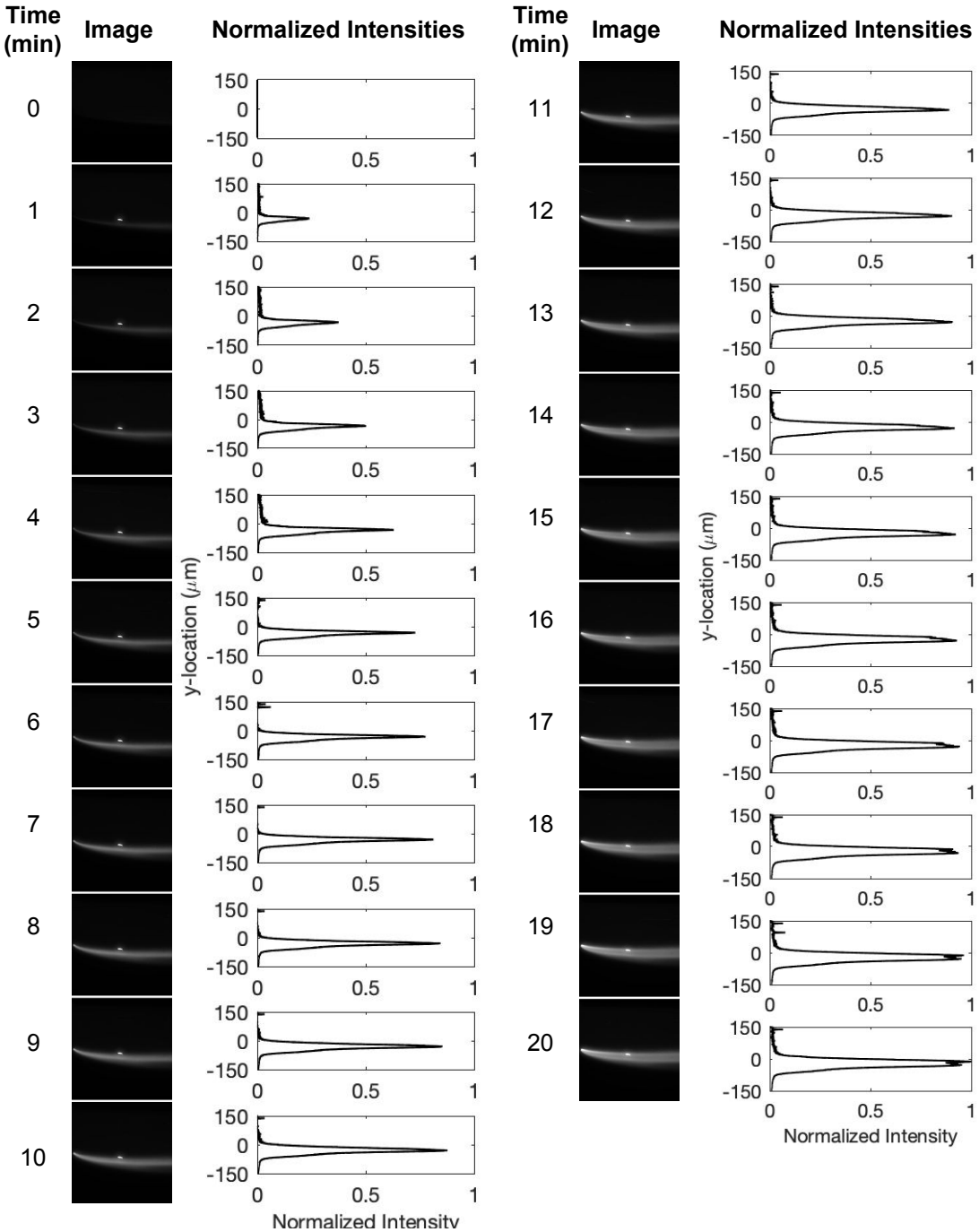

400 nL/min - Run 1

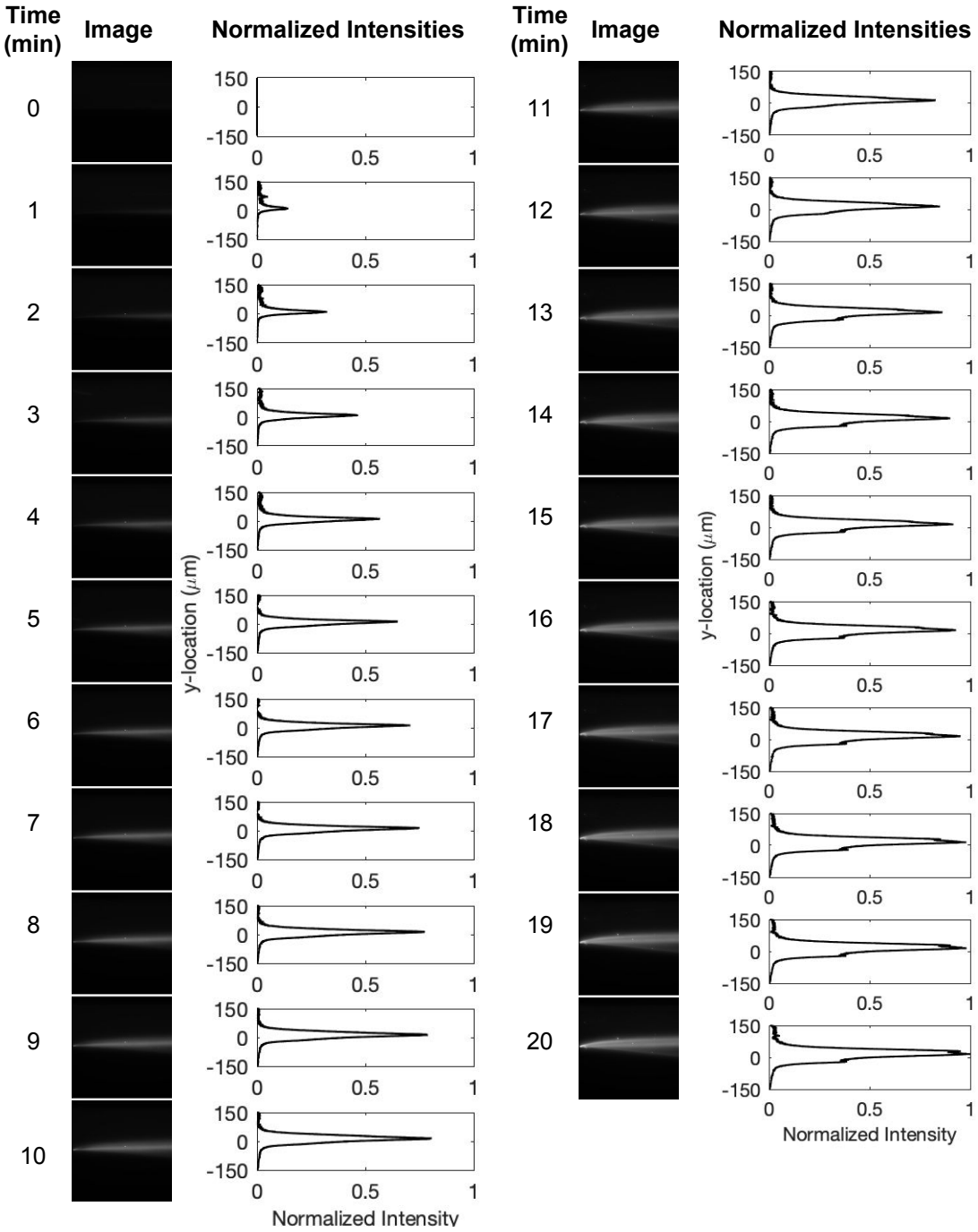

400 nL/min - Run 2

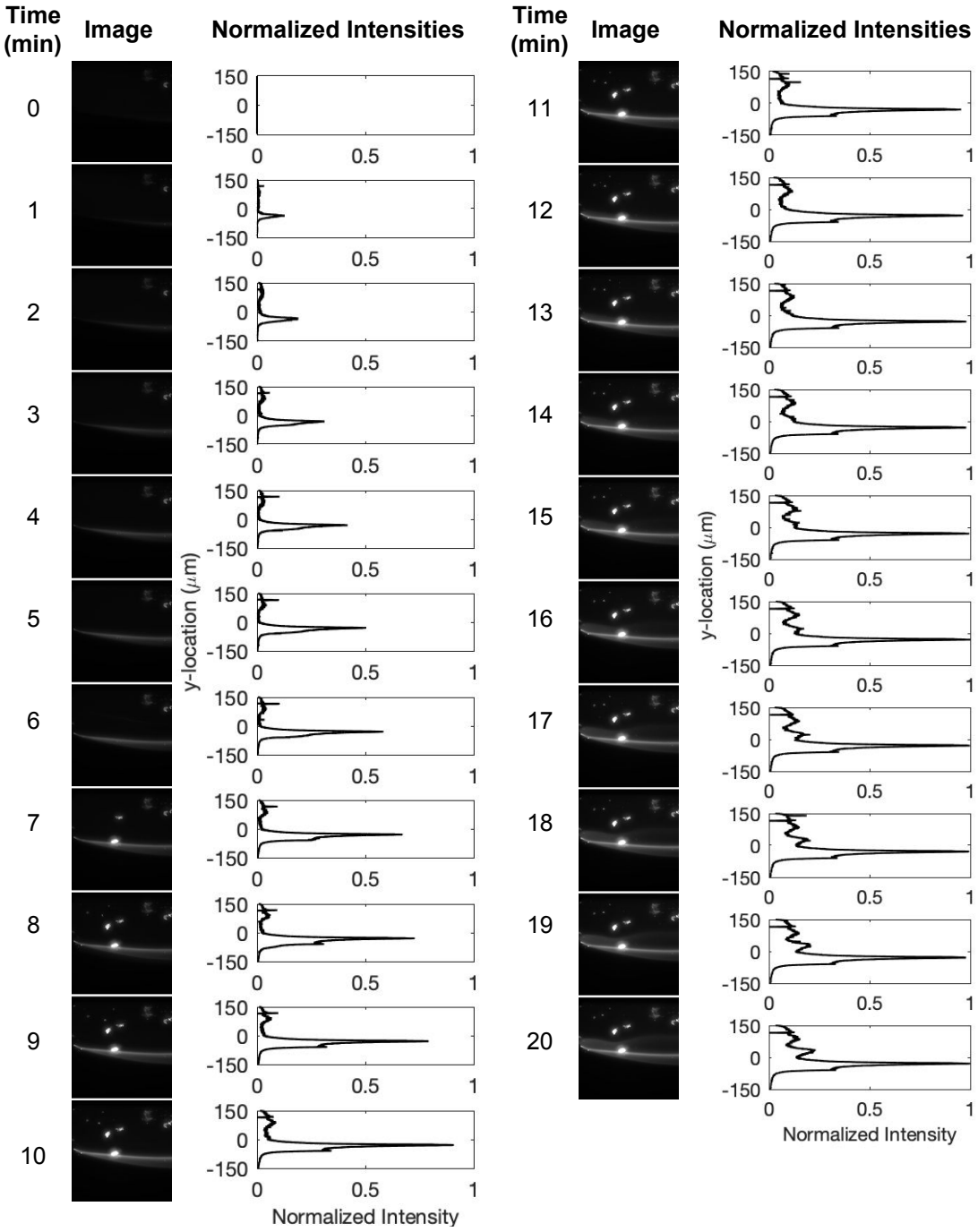

APPENDIX B: MATLAB CODE FOR IMAGE ANALYSIS

Extracting Intensity Data and Maximum Intensity Curve Fit

```
%pixel range for profile locations
loc_x=([2166 333; 2173 340; 2233 400; 2168 335; 1986 153; 1953 120]);
%297.72 µm length
loc_y=([1900 1900; 1928 1928; 1888 1888; 1892 1892; 1972 1972; 1925
1925]); %at 300 µm from inlet
t0=[0 1 0 0 1 1]; %starting time in minutes
duration=20; %in minutes

d=dir('*.tif'); %importing all tif files

%graph plot dimensions
figure_height = 256;
figure_width = 4*figure_height/3; %set aspect ratio
font_size = figure_height/24; %scale text proportionally

% set scale
scale = 415.84/2560; %pixels in µm for 40X objective

for i=1:numel(d) %working through the different stacks

    %extracting intensity profiles from a stack of images

    fname=d(i).name;
    info = imfinfo(fname);
    num_images = numel(info); %number of images in the stack

    %insert line location for intensity profile
    x = loc_x(i,:);
    y = loc_y(i,:);

    for k = t0(i)+1:(t0(i)+duration+1) %images within the stack

        I = imread(fname, k);
        [cx,cy,YofIntensity]=improfile(I,x,y);

        if k == t0(i)+1
            intensity_0 = YofIntensity;
        end

        intensity(:,k-t0(i),i)=YofIntensity-intensity_0; %calibrate

        max_intensity(k-t0(i),i)=max(intensity(:,k-t0(i),i));
        t(k-t0(i),i) = k-t0(i)-1;

    end
```

```
max_intensity_norm(:,i)=max_intensity(:,i)/max(max_intensity(:,i));%norma
lized by maximum intensity

end

%curve fit for maximum intensity
for i=1:numel(d)

    y_max = max(max_intensity_norm(:,i));
    x = t(:,i);
    y = max_intensity_norm(:,i);
    n = length(y);

    model = @(c,x) c(1)*(1-exp(-c(2)*x));
    c0 = [0,0.1];  % Seed value.
    [c,resnorm] = lsqcurvefit(model,c0,x,y);
    y_fit(:,i) = c(1)*(1-exp(-c(2)*x));

    SSR = 0;
    SST = 0;
    t_c(i)=1/c(2) %time constant
    y_avg = mean(y)
    for j = 1:n
        SSR = SSR + (y_fit(j)-y_avg)^2;
        SST = SST + (y(j)-y_avg)^2;
    end
    r_squared = SSR/SST

    text_string = sprintf('y = %.2f*(1-exp(-%.3f*x))\nR² = %.3f',
c(1),c(2),r_squared)
    a(:,i)=c';

end
```

Extracting Shape Parameters

```
y_norm = -((cx-(min(cx)))*scale-150)/300; %normalizing width
n_start = 4; %there are no peaks in the first few minutes
cut=0.25; %intensity lower threshold

%graph plot dimensions
figure_height = 256/2;
figure_width = 4*256/3; %set aspect ratio
font_size = 256/24; %scale text proportionally

for i=1:numel(d)

    intensity_norm(:,:,i)=intensity(:,:,i)/max(max_intensity(:,i));
%normalizing intensity

    for j=n_start:duration+1 %finding locations of triangular points

        [maxValue,Ind_max]=max(intensity_norm(:,j,i));
        [minValue,Ind_1(j,i)] =
min(abs(intensity_norm(1:Ind_max-1,j,i)-cut));
        [minValue_2,Ind_2(j,i)] =
min(abs(intensity_norm(Ind_max+1:length(y_norm),j,i)-cut));
        Ind_2(j,i) = Ind_max+Ind_2(j,i);

        del_int = max(intensity_norm(:,j,i))-cut;
        del_y_1 = y_norm(Ind_max)-y_norm(Ind_1(j,i));
        del_y_2 = y_norm(Ind_2(j,i))-y_norm(Ind_max);


acute(j-n_start+1,i)=atand(del_y_1/del_int)+atand(del_y_2/del_int); %in
degrees

        theta_max=max([atand(del_int/del_y_1), atand(del_int/del_y_2)]);
        theta_min=min([atand(del_int/del_y_1), atand(del_int/del_y_2)]);

        asym(j-n_start+1,i)=theta_min/theta_max;


skew_cut(j-n_start+1,i)=skewness(intensity(Ind_1(j,i):Ind_2(j,i),j,i));
%calculating skewness on selected region

kurt_cut(j-n_start+1,i)=kurtosis(intensity(Ind_1(j,i):Ind_2(j,i),j,i));
%calculating kurtosis on selected region

    end

end
```